

1 **Back-calculation of the 2017 Piz Cengalo-Bondo landslide cas-
2 cade with r.avaflow**

3 ***Martin Mergili^{1,2}, Michel Jaboiedoff³, José Pullarello³, Shiva P. Pudasaini⁴***

4 ¹ Institute of Applied Geology, University of Natural Resources and Life Sciences (BOKU), Peter-Jordan-
5 Straße 82, 1190 Vienna, Austria

6 ² Geomorphological Systems and Risk Research, Department of Geography and Regional Research, Uni-
7 versity of Vienna, Universitätsstraße 7, 1010 Vienna, Austria

8 ³Institute of Earth Sciences, University of Lausanne, Quartier UNIL-Mouline, Bâtiment Géopolis, 1015
9 Lausanne, Switzerland

10 ⁴ Institute of Geosciences, Geophysics Section, University of Bonn, Meckenheimer Allee 176, 53115
11 Bonn, Germany

12 Correspondence to: M. Mergili (martin.mergili@boku.ac.at)

13 **Abstract**

14 In the morning of 23 August 2017, around 3 million m³ of granitoid rock broke off from the east face of
15 Piz Cengalo, SE Switzerland. The initial rock slide-rock fall entrained 0.6 million m³ of a glacier and
16 continued as a rock(-ice) avalanche, before evolving into a channelized debris flow that reached the
17 village of Bondo at a distance of 6.5 km after a couple of minutes. Subsequent debris flow surges fol-
18 lowed in the next hours and days. The event resulted in eight fatalities along its path and severely dam-
19 aged Bondo. The most likely candidates for the water causing the transformation of the rock avalanche
20 into a long-runout debris flow are the entrained glacier ice and water originating from the debris be-
21 neath the rock avalanche. In the present work we try to reconstruct conceptually and numerically the
22 cascade from the initial rock slide-rock fall to the first debris flow surge and thereby consider two sce-
23 narios in terms of qualitative conceptual process models: (i) entrainment of most of the glacier ice by the
24 frontal part of the initial rock slide-rock fall and/or injection of water from the basal sediments due to
25 sudden rise in pore pressure, leading to a frontal debris flow, with the rear part largely remaining dry
26 and depositing mid-valley; and (ii) most of the entrained glacier ice remaining beneath/behind the
27 frontal rock avalanche, and developing into an avalanching flow of ice and water, part of which overtops
28 and partially entrains the rock avalanche deposit, resulting in a debris flow. Both scenarios can – with
29 some limitations – be numerically reproduced with the two-phase mass flow model (Pudasaini, 2012)
30 implemented with the simulation software r.avaflow, based on plausible assumptions of the model pa-
31 rameters. However, these simulation results do not allow to conclude on which of the two scenarios is
32 the more likely one. Future work will be directed towards the application of a three-phase flow model

33 (rock, ice, fluid) including phase transitions, in order to better represent the melting of glacier ice, and a
34 more appropriate consideration of deposition of debris flow material along the channel.

35 Keywords: Debris flow, Entrainment, High-mountain process chain, Rock avalanche, Two-phase flow
36 model, r.avaflow

37 **1 Introduction**

38 Landslides lead to substantial damages to life, property, and infrastructures every year. Whereas initial
39 landslides in hilly terrain have mostly local effects, landslides in high-mountain areas, with elevation
40 differences of thousands of metres over a few kilometres may form the initial points of process chains
41 which, due to their interactions with glacier ice, snow, lakes, or basal material, sometimes evolve into
42 long-runout debris avalanches, debris flows or floods. Such complex landslide events may occur in re-
43 mote areas, such as the 2012 Alpl rock-snow avalanche in Austria (Preh and Sausgruber, 2015) or the
44 2012 Santa Cruz multi-lake outburst event in Peru (Mergili et al., 2018a). If they reach inhabited areas,
45 such events lead to major destruction even several kilometres away from the source and have led to ma-
46 jor disasters in the past, such as the 1949 Khait rock avalanche-loess flow in Tajikistan (Evans et al.,
47 2009b); the 1962 and 1970 Huascarán rock fall-debris avalanche events in Peru (Evans et al., 2009a;
48 Mergili et al., 2018b); the 2002 Kolka-Karmadon ice-rock avalanche in Russia (Huggel et al., 2005); the
49 2012 Seti River debris flood in Nepal (Bhandari et al., 2012); or the 2017 Piz Cengalo-Bondo rock ava-
50 lanche-debris flow event in Switzerland. The initial fall or slide sequences of such process chains are
51 commonly related to a changing cryosphere such as glacial debuttressing, the formation of hanging gla-
52 ciers, or a changing permafrost regime (Harris et al., 2009; Krautblatter et al., 2013; Haeberli and
53 Whiteman, 2014; Haeberli et al., 2017).

54 Computer models assist risk managers in anticipating the impact areas, energies, and travel times of
55 complex mass flows. Conventional single-phase flow models, considering a mixture of solid and fluid
56 components (e.g. Voellmy, 1955; Savage and Hutter, 1989; Iverson, 1997; McDougall and Hungr, 2004;
57 Christen et al., 2010), do not serve for such a purpose. Instead, simulations rely on (i) model cascades,
58 changing from one approach to the next at each process boundary (Schneider et al., 2014; Somos-
59 Valenzuela et al., 2016); or (ii) bulk mixture models or two- or even multi-phase flow models (Pit-
60 man and Le, 2005; Pudasaini, 2012; Iverson and George, 2014; Mergili et al., 2017). Worni et al. (2014)
61 have highlighted the advantages of (ii) for considering also the process interactions and boundaries.
62 Two- or multi-phase flow models separately consider the solid and the fluid phase, but also phase inter-
63 actions.

64 The aim of the present work is to learn about our ability to reproduce sophisticated transformation
65 mechanisms involved in complex, cascading landslide processes, with GIS-based tools. For this purpose,
66 we apply the computational tool `r.avaflow` (Mergili et al., 2017), which employs an enhanced version of
67 the Pudasaini (2012) two-phase flow model, to back-calculate the 2017 Piz Cengalo-Bondo landslide
68 cascade in SE Switzerland, which was characterized by the transformation of a rock avalanche to a long-
69 runout debris flow. We consider two scenarios in terms of hypothetic qualitative conceptual models of
70 the physical transformation mechanisms. On this basis, we try to numerically reproduce these scenarios,
71 satisfying the requirements of physical plausibility of the model parameters, and empirical adequacy in
72 terms of correspondence of the results with the documented and inferred impact areas, volumes, veloc-
73 ities, and travel times. Based on the outcomes, we identify the key challenges to be addressed in future
74 research.

75 Thereby we rely on the detailed description, documentation, and topographic reconstruction of this
76 recent event. The event documentation, data used, and the conceptual models are outlined in Section 2.
77 We briefly introduce the simulation framework `r.avaflow` (Section 3) and explain its parametrization
78 and our simulation strategy (Section 4) before presenting (Section 5) and discussing (Section 6) the re-
79 sults obtained. Finally, we conclude with the key messages of the study (Section 7).

80 **2 The 2017 Piz Cengalo-Bondo landslide cascade**

81 **2.1 Piz Cengalo and Val Bondasca**

82 The Val Bondasca is a left tributary valley to the Val Bregaglia in the canton of the Grisons in SE Swit-
83 zerland (Fig. 1). The Bondasca stream joins the Mera River at the village of Bondo at 823 m asl. It drains
84 part of the Bregaglia Range, built up by a mainly granitic intrusive body culminating at 3678 m asl. Piz
85 Cengalo, with a summit elevation of 3368 m asl, is characterized by a steep, intensely fractured NE face
86 which has repeatedly been the scene of landslides, and which is geomorphologically connected to the
87 Val Bondasca through a steep glacier forefield. The glacier itself has largely retreated to the cirque be-
88 neath the rock wall.

89 On 27 December 2011, a rock avalanche with a volume of 1.5–2 million m³ developed out of a rock top-
90 pling from the NE face of Piz Cengalo, travelling for a distance of 1.5 km down to the uppermost part of
91 the Val Bondasca (Haeberli et al., 2013; De Blasio and Crosta, 2016; Amann et al., 2018). This rock ava-
92 lanche reached the main torrent channel. Erosion of the deposit thereafter resulted in increased debris
93 flow activity (Frank et al., 2019). No entrainment of glacier ice was documented for this event. As blue
94 ice had been observed directly at the scarp, the role of permafrost for the rock instability was discussed.

95 An early warning system was installed and later extended (Steinacher et al., 2018). Displacements at the
96 scarp area, measured by radar interferometry and laser scanning, were few centimetres per year between
97 2012 and 2015, and accelerated in the following years. In early August 2017, increased rock fall activity
98 and deformation rates alerted the authorities. A major rock fall event occurred on 21 August 2017
99 (Amann et al., 2018).

100 **2.2 The event of 23 August 2017**

101 The complex landslide which occurred on 23 August 2017 was documented mainly by reports of the
102 Swiss Federal Institute for Forest, Snow and Landscape Research (WSL), the Laboratory of Hydraulics,
103 Hydrology and Glaciology (VAW) of the ETH Zurich, and the Amt für Wald und Naturgefahren (Office
104 for Forest and Natural Hazards) of the canton of Grisons.

105 At 9:31 am local time, a volume of approx. 3 million m³ detached from the NE face of Piz Cengalo, as
106 indicated by WSL (2017); Amann et al. (2018); and the point cloud we obtained through structure from
107 motion using pictures taken after the event. Documented by videos and by seismic records (Walter et al.,
108 2018), it impacted the glacier beneath the rock face and entrained approx. 0.6 million m³ of ice (VAW,
109 2017; WSL, 2017), was sharply deflected at an opposite rock wall, and evolved into a rock(-ice) ava-
110 lanche. Part of this avalanche immediately converted into a debris flow which flowed down the Val
111 Bondasca. It was detected at 9:34 by the debris flow warning system which had been installed near the
112 hamlet of Prä approx. 1 km upstream from Bondo. According to different sources, the debris flow surge
113 arrived at Bondo between 9:42 (derived from WSL, 2017) and 9:48 (Amt für Wald und Naturgefahren,
114 2017). The rather low velocity in the lower portion of the Val Bondasca is most likely a consequence of
115 the narrow gorge topography, and of the viscous behaviour of this first surge. Whereas approx.
116 540,000 m³ of material were involved, only 50,000 m³ arrived at Bondo immediately (data from the Can-
117 ton of Grisons reported by WSL, 2017). The remaining material was partly remobilized by six further
118 debris flow surges recorded during the same day, one on 25 August, and one – triggered by rainfall – on
119 31 August 2017. All nine surges together deposited a volume of approx. 500,000–800,000 m³ in the area
120 of Bondo, less than half of which was captured by a retention basin (Bonanomi and Keiser, 2017).

121 The vertical profile of the main flow path is illustrated in Fig. 4. The total angle of reach of the process
122 chain from the initial release down to the outlet of the Bondasca Valley was approx. 17.4°, computed
123 from the travel distance of 7.0 km and the vertical drop of approx. 2.2 km. The initial landslide to the
124 terminus of the rock avalanche showed an angle of reach of approx. 25.8°, derived from the travel dis-
125 tance of 3.4 km and the vertical drop of 1.7 km. This value is higher than the 22° predicted by the equa-
126 tion of Scheidegger (1973), probably due to the sharp deflection of the initial landslide. Following the

127 concept of Nicoletti and Sorriso-Valvo (1991), the rock avalanche was characterized by channelling of
128 the mass. Only a limited run-up was observed, probably due to the gentle horizontal curvature of the
129 valley in that area (no orthogonal impact on the valley slope; Hewitt, 2002). There were eight fatalities,
130 concerning hikers in the Val Bondasca, extensive damages to buildings and infrastructures, and evacua-
131 tions for several weeks or even months.

132 **2.3 Data and conceptual model**

133 Reconstruction of the rock and glacier volumes involved in the event was based on an overlay of a 2011
134 swisstopo MNS-Digital Elevation Model (DEM) (contract: swisstopo–DV084371), derived through air-
135 borne laser scanning in 2011 and available at a raster cell size of 2 m, and a Digital Surface Model (DSM)
136 obtained through Structure from Motion (SfM) techniques after the 2017 event. This analysis resulted in
137 a detached rock volume of 3.27 million m³, which is slightly more than the value of 3.15 million m³
138 reported by Amann et al. (2018), and an entrained ice volume of 770,000 m³ (Fig. 5). However, these
139 volumes neglect smaller rock falls before and after the large 2017 event, and also glacial retreat. The
140 2011 event took place after the DTM had been acquired, but it released from an area above the 2017
141 scarp. The boundary between the 2011 and the 2017 scarps, however, is slightly uncertain, which ex-
142 plains the discrepancies between the different volume reconstructions. Assuming some minor entrain-
143 ment of the glacier ice in 2011 and some glacial retreat, we arrive at an entrained ice volume of
144 600,000 m³, a value which is very well supported by VAW (2017).

145 There is still disagreement on the origin of the water having led to the debris flow, particularly to the
146 first surge. Bonanomi and Keiser (2017) clearly mention meltwater from the entrained glacier ice as the
147 main source, whereby much of the melting is assigned to impact, shearing and frictional heating directly
148 at or after impact, as it is often the situation in rock-ice avalanches (Pudasaini and Krautblatter, 2014).
149 WSL (2017) has shown, however, that the energy released was only sufficient to melt approx. half of the
150 glacier ice. Water pockets in the glacier or a stationary water source along the path might have played
151 an important role (Demmel, 2019). Walter et al. (2019) claim that much of the glacier ice was crushed,
152 ejected and dispersed (Fig. 3b), whereas water injected into the rock avalanche due to pore pressure rise
153 in the basal sediments would have played a major role. In any case, the development of a debris flow
154 from a landslide mass with an overall solid fraction of as high as ~0.85 (considering the water equivalent
155 of the glacier ice) requires some spatio-temporal differentiation of the water/ice content. We consider
156 two qualitative conceptual models – or scenarios – possibly explaining such a differentiation:

157 S1 The initial rock slide-rock fall led to massive entrainment, fragmenting and melting of glacier
158 ice, mixing of rock with some of the entrained ice and the meltwater, and injection of water

159 from the basal sediments into the rock avalanche mass quickly upon impact due to overload-
160 induced pore pressure rise. As a consequence, the front of the rock avalanche was characterized
161 by a high content of ice and water, highly mobile, and therefore escaped as the first debris flow
162 surge, whereas the less mobile rock avalanche behind – still with some water and ice in it – de-
163 celerated and deposited mid-valley. The secondary debris flow surges occurred mainly due to
164 backwater effects. This scenario largely follows the explanation of Walter et al. (2019) that the
165 first debris flow surge was triggered at the front of the rock avalanche by overload and pore
166 pressure rise, whereas the later surges overtopped the rock avalanche deposits, as indicated by
167 the surficial scour patterns.

168 S2 The initial rock slide-rock fall impacted and entrained the glacier. Most of the entrained ice re-
169 mained beneath and developed into an avalanching flow of melting ice behind the rock ava-
170 lance. The rock avalanche decelerated and stopped mid-valley. Part of the avalanching flow
171 overtopped and partly entrained the rock avalanche deposit – leaving behind the scour traces ob-
172 served in the field – and evolved into the channelized debris flow which arrived at Bondo a cou-
173 ple of minutes later. The secondary debris flow surges started from the rock avalanche deposit
174 due to melting and infiltration of the remaining ice, and due to backwater effects. This scenario
175 is similar to the theory developed at the WSL Institute for Snow and Avalanche Research (SLF),
176 who also did a first simulation of the rock avalanche (WSL, 2017).

177 Fig. 6 illustrates the conceptual models attempting to explain the key mechanisms involved in the rock
178 avalanche-debris flow transformation.

179 3 The simulation framework r.avaflow

180 r.avaflow represents a comprehensive GIS-based open source framework which can be applied for the
181 simulation of various types of geomorphic mass flows. In contrast to most other mass flow simulation
182 tools, r.avaflow utilizes a general two-phase-flow model describing the dynamics of the mixture of solid
183 particles and viscous fluid and the strong interactions between these phases. It further considers erosion
184 and entrainment of surface material along the flow path. These features facilitate the simulation of cas-
185 cading landslide processes such as the 2017 Piz Cengalo-Bondo event. r.avaflow is outlined in full detail
186 by Mergili and Pudasaini (2019). The code, a user manual, and a collection of test datasets are available
187 from Mergili (2019). Only those aspects directly relevant for the present work are described in this sec-
188 tion.

189 Essentially, the Pudasaini (2012) two-phase flow model is employed for computing the dynamics of mass
190 flows moving from a defined release area (solid and/or fluid heights are assigned to each raster cell) or
191 release hydrograph (at each time step, solid and/or fluid heights are added at a given profile, moving at a
192 given cross-profile velocity) down through a DEM. The spatio-temporal evolution of the flow is approx-
193 imated through depth-averaged solid and fluid mass and momentum balance equations (Pudasaini,
194 2012). This system of equations is solved through the TVD-NOC Scheme introduced by Nessyahu and
195 Tadmor (1990), adapting an approach presented by Tai et al. (2002) and Wang et al. (2004). The charac-
196 teristics of the simulated flow are governed by a set of flow parameters (some of them are shown in the
197 Tables 1 and 2). Compared to the Pudasaini (2012) model, some extensions have been introduced which
198 include (i) ambient drag or air resistance (Kattel et al., 2016; Mergili et al., 2017); and (ii) fluid friction,
199 governing the influence of basal surface roughness on the fluid momentum (Mergili et al., 2018b). Both
200 extensions rely on empirical coefficients, C_{AD} for the ambient drag and C_{FF} for the fluid friction. Further,
201 drag and viscosity are computed according to enhanced concepts. As in Domnik et al. (2013) and Puda-
202 saini and Mergili (2019), the fluid viscosity is enhanced by the yield strength. Most importantly, the
203 internal friction angle φ and the basal friction angle δ of the solid are scaled with the solid fraction in
204 order to approximate effects of reduced interaction between the solid particles and the basal surface in
205 fluid-rich flows.

206 Entrainment is calculated through an empirical model. In contrast to Mergili et al. (2017), where an em-
207 pirical entrainment coefficient is multiplied with the momentum of the flow, here we multiply the en-
208 trainment coefficient C_E ($\text{s kg}^{-1} \text{ m}^{-1}$) with the kinetic energy of the flow:

$$209 \quad q_{E,s} = C_E |T_s + T_f| \alpha_{s,E}, \quad q_{E,f} = C_E |T_s + T_f| (1 - \alpha_{s,E}), \quad (1)$$

210 where $q_{E,s}$ and $q_{E,f}$ (m s^{-1}) are the solid and fluid entrainment rates, T_s and T_f (J) are the kinetic energies of
211 the solid and fluid fractions of the flow, and $\alpha_{s,E}$ is the solid fraction of the entrainable material. Solid
212 and fluid flow heights and momenta, and the change of the basal topography, are updated at each time
213 step (see Mergili et al., 2017 for details).

214 As r.avaflow operates on the basis of GIS raster cells, its output essentially consists of raster maps –for all
215 time steps and for the overall maximum – of solid and fluid flow heights, velocities, pressures, kinetic
216 energies, and entrained heights. In addition, output hydrograph profiles may be defined at which solid
217 and fluid heights, velocities, and discharges are provided at each time step.

218 **4 Parameterization of r.avaflow**

219 One set of simulations is performed for each of the Scenarios S1 and S2 (Fig. 6), considering the process
220 chain from the release of the rock slide-rock fall to the arrival of the first debris flow surge at Bondo.
221 Neither triggering of the event nor subsequent surges or distal debris floods beyond Bondo are consid-
222 ered in this study. Equally, the dust cloud associated to the rock avalanche (WSL, 2017) is not the subject
223 here. Initial sliding of the glacier beneath the rock avalanche, as assumed in Scenario S2, cannot directly
224 be modelled. That would require a three-phase model, which is beyond the scope here. Instead, release
225 of the glacier ice and meltwater is assumed in a separate simulation after the rock avalanche has passed
226 over it. We consider this workaround an acceptable approximation of the postulated scenario (Sec-
227 tion 6).

228 We use the 2011 swisstopo MNS-DEM, corrected for the rock slide-rock fall scarp and the entrained
229 glacier ice by overlay with the 2017 SfM DSM (Section 2). The maps of release height and maximum
230 entrainable height are derived from the difference between the 2011 swisstopo DTM and the 2017 SfM
231 DSM (Fig. 5; Section 2). The release mass is considered completely solid, whereas the entrained glacier is
232 assumed to contain some solid fraction (coarse till). The glacier ice is assumed to melt immediately on
233 impact and is included in the fluid along with fine till. We note that the fluid phase does not represent
234 pure water, but a mixture of water and fine particles (Table 2). The fraction of the glacier allowed to be
235 incorporated in the process chain is empirically optimized (Table 3). Based on the same principle, the
236 maximum depth of entrainment of fluid due to pore pressure overload in Scenario S1 is set to 25 cm,
237 whereas the maximum depth of entrainment of the rock avalanche deposit in Scenario S2 is set to 1 m.

238 The study area is divided into six zones A–F (Fig. 4 and Fig. 7; Table 1). Each of these zones represents
239 an area with particular geomorphic characteristics and dominant process types, which can be translated
240 into model parameters. Due to the impossibility to directly measure the key parameters in the field
241 (Mergili et al., 2018a, b), the parameters summarized in Table 1 and Table 2 are the result of an iterative
242 optimization procedure, where multiple simulations with different parameter sets are performed in or-
243 der to arrive at one “optimum” simulation for each scenario. It is thereby important to note that we
244 largely derive one single set of optimized parameters, which is valid for both of the scenarios. Optimiza-
245 tion criteria are (i) the empirical adequacy of the model results, and (ii) the physical plausibility of the
246 parameters. Thereby, the empirical adequacy is quantified through comparison of the results with the
247 documented impact area, the travel times to the output hydrograph profiles O2, O3, and O4 (Fig. 7), and
248 the reported volumes (Amt für Wald und Naturgefahren, 2017; Bonanomi and Keiser, 2017; WSL, 2017).
249 The physical plausibility of the model parameters is evaluated on the basis on the parameters suggested

250 by Mergili et al. (2017) and on the findings of Mergili et al. (2018a, b). The values of the basal friction
251 angle (δ), the ambient drag coefficient (C_{AD}), the fluid friction coefficient (C_{FF}), and the entrainment
252 coefficient (C_E) are differentiated between and within the zones (Table 1), whereas global values are
253 defined for all the other parameters (Table 2). It is further important to note that δ scales linearly with
254 the solid fraction – this means that the values given in Table 1 only apply for 100% solid.

255 Durations of $t = 1800$ s are considered for both scenarios. At this point of time, the first debris flow surge
256 has largely passed and left the area of interest, except for some remaining tail of fluid material. Only
257 heights ≥ 0.25 m are taken into account for the visualization and evaluation of the simulation results. A
258 threshold of 0.001 m is used for the simulation itself, keeping the loss due to numerical diffusion within
259 a range of <1–4% until the point when the flow first leaves the area of interest. Considering the size of
260 the event, a cell size of 10 m is considered the best compromise between capturing a sufficient level of
261 detail and ensuring an adequate computational efficiency, and is therefore applied for all simulations.

262 5 Simulation results

263 5.1 Scenario S1 – Frontal debris flow surge

264 Fig. 8 illustrates the distribution of the simulated maximum flow heights, maximum entrained heights,
265 and deposition area after $t = 1800$ s, when most of the initial debris flow surge has passed the confluence
266 of the Bondasca stream and the Maira river. The comparison of observed and simulated impact areas
267 results in a critical success index $CSI = 0.558$, a distance to perfect classification $D2PC = 0.167$, and a fac-
268 tor of conservativeness $FoC = 1.455$. These performance indicators are derived from the confusion matrix
269 of true positives, true negatives, false positives, and false negatives. CSI and $D2PC$ measure the corre-
270 spondence of the observed and simulated impact areas. Both indicators can range between 0 and 1,
271 whereby values of CSI close to 1 and values of $D2PC$ close to 0 point to a good correspondence. FoC in-
272 dicates whether the observed impact areas are overestimated ($FoC > 1$), or underestimated by the simu-
273 lation ($FoC < 1$). More details are provided by Formetta et al. (2015) and by Mergili et al. (2017, 2018a).

274 Interpreting these values as indicators for a reasonably good correspondence between simulation and
275 observation in terms of impact area, we now consider the dimension of time, focussing on the output
276 hydrographs OH1–OH4 (Fig. 9; see Fig. 7 and Fig. 8 for the location of the corresponding hydrograph
277 profiles O1–O4). Much of the rock avalanche passes the profile O1 between $t = 60$ s and $t = 100$ s. OH2
278 (Fig. 9a; located in the upper portion of Val Bondasca) sets on before $t = 140$ s and quickly reaches its
279 peak, with a volumetric solid ratio of approx. 30% (maximum 900 m³/s of solid and 2,200 m³/s of fluid
280 discharge). Thereafter, this first surge quickly tails off. The solid flow height, however, increases to

281 around 3 m and remains so until the end of the simulation, whereas the fluid flow height slowly and
282 steadily tails off. Until $t = 1800$ s the profile O2 is passed by a total of 221,000 m³ of solid and 308,000 m³
283 of fluid material (the fluid representing a mixture of fine mud and water with a density of 1,400 kg m⁻³;
284 see Table 2). The hydrograph profile O3 in Prä, approx. 1 km upstream of Bondo, is characterized by a
285 surge starting before $t = 280$ s and slowly tailing off afterwards. Discharge at the hydrograph OH4
286 (Fig. 9b; O4 is located at the outlet of the canyon to the debris fan of Bondo) starts at around $t = 700$ s
287 and reaches its peak of solid discharge at $t = 1020$ s (167 m³/s). Solid discharge decreases thereafter,
288 whereas the flow becomes fluid-dominated with a fluid peak of 202 m³/s at $t = 1320$ s. The maximum
289 total flow height simulated at O4 is 2.53 m. This site is passed by a total of 91,000 m³ of solid and
290 175,000 m³ of fluid material, according to the simulation – an overestimate, compared to the documenta-
291 tion (Table 3).

292 Fig. 10 illustrates the travel time and the frontal velocities of the rock avalanche and the initial debris
293 flow. The initial surge reaches the hydrograph profile O3 – located 1 km upstream of Bondo – at
294 $t = 280$ s (Fig. 10a; Fig. 9c). This is in line with the documented arrival of the surge at the nearby moni-
295 toring station (Table 3). Also the simulated travel time to the profile O4 corresponds to the – though
296 uncertain – documentation. The initial rock avalanche is characterized by frontal velocities >25 m/s,
297 whereas the debris flow largely moves at 10–25 m/s. Velocities drop below 5 m/s in the lower part of the
298 valley (Zone E) (Fig. 10b).

299 5.2 Scenario S2 – Debris flow surge by overtopping and entrainment of rock avalanche

300 Fig. 11 illustrates the distribution of the simulated maximum flow heights, maximum entrained heights,
301 and deposition area after $t = t_0 + 1740$ s, where t_0 is the time between the release of the initial rock ava-
302 lanche and the mobilization of the entrained glacier. The simulated impact and deposition areas of the
303 initial rock avalanche are also shown in Fig. 11. However, we now concentrate to the debris flow, trig-
304 gered by the entrainment of 145,000 m³ of solid material from the rock avalanche deposit. Flow heights
305 – as well as the hydrographs presented in Fig. 9c and d and the temporal patterns illustrated in Fig. 12 –
306 only refer to the debris flow developing from the entrained glacier and the entrained rock avalanche
307 material. The confusion matrix of observed and simulated impact areas reveals partly different patterns
308 of performance than for the Scenario S1: $CSI = 0.590$; $D2PC = 0.289$; and $FoC = 0.925$. The lower FoC
309 value and the lower performance in terms of $D2PC$ reflect the missing initial rock avalanche in the
310 simulation results. The output hydrographs OH2 and OH4 differ from the hydrographs obtained
311 through the Scenario S1, but also show some similarities (Fig. 9c and d). Most of the flow passes through
312 the hydrograph profile O1 between $t = t_0 + 40$ s and $t_0 + 80$ s, and through O2 between $t = t_0 + 100$ s and

313 $t_0 + 180$ s. The hydrograph OH2 is characterized by a short peak of 3,500 m³/s of solid and 4,500 m³/s of
314 fluid, with a volumetric solid fraction of 0.44 and quickly decreasing discharge afterwards (Fig. 9c). In
315 contrast to Scenario S1, flow heights drop steadily, with values below 2 m from $t = t_0 + 620$ s onwards.
316 The hydrograph OH3 is characterized by a surge starting around $t = t_0 + 240$ s. Discharge at the hydro-
317 graph OH4 (Fig. 9d) sets on around $t = t_0 + 600$ s, and the solid peak of 240 m³/s is simulated at approx.
318 $t = t_0 + 780$ s. The delay of the peak of fluid discharge is more pronounced when compared to Scenario S1
319 (310 m³/s at $t = t_0 + 960$ s). Profile O4 is passed by a total of 65,000 m³ of solid and 204,000 m³ of fluid
320 material. The volumetric solid fraction drops from above 0.60 at the very onset of the hydrograph to
321 around 0.10 (almost pure fluid) at the end. The maximum total flow height at O4 is 3.1 m.

322 Fig. 12 illustrates the travel times and the frontal velocities of the rock avalanche and the initial debris
323 flow. Assuming that t_0 is in the range of some tens of seconds, the time of arrival of the surge at O3 is in
324 line with the documentation also for the Scenario S2 (Fig. 12a; Table 3). The frontal velocity patterns
325 along Val Bondasca are roughly in line with those derived in the Scenario S1 (Fig. 12b). However, the
326 scenarios differ among themselves in terms of the more pronounced, but shorter peaks of the hydro-
327 graphs in Scenario S2 (Fig. 9). This pattern is a consequence of the more sharply defined debris flow
328 surge. In Scenario S1, the front of the rock avalanche deposit constantly “leaks” into Val Bondasca,
329 providing supply for the debris flow also at later stages. In Scenario S2, entrainment of the rock ava-
330 lanche deposit occurs relatively quickly, without material supply afterwards. This type of behaviour is
331 strongly coupled to the value of C_E and the allowed height of entrainment chosen for the rock avalanche
332 deposit.

333 6 Discussion

334 Our simulation results reveal a reasonable degree of empirical adequacy and physical plausibility with
335 regard to most of the reference observations. Having said that, we have also identified some important
336 limitations which are now discussed in more detail. First of all, we are not able to decide on the more
337 realistic of the two Scenarios S1 and S2. In general, the melting and mobilization of glacier ice upon rock
338 slide-rock fall impact is hard to quantify from straightforward calculations of energy transformation, as
339 Huggel et al. (2005) have demonstrated on the example of the 2002 Kolka-Karmadon event. In the pre-
340 sent work, the assumed amount of melting (approx. half of the glacier ice) leading to the empirically
341 most adequate results corresponds well to the findings of WSL (2017), indicating a reasonable degree of
342 plausibility. It remains equally difficult to quantify the amount of water injected into the rock avalanche
343 by overload of the sediments and the resulting pore pressure rise (Walter et al., 2019). Confirmation or

344 rejection of conceptual models with regard to the physical mechanisms involved in specific cases would
345 have to be based on better constrained initial conditions, and the availability of robust parameter sets.

346 We note that with the approach chosen we are not able (i) to adequately simulate the transition from
347 solid to fluid material; and (ii) to consider rock and ice separately with different material properties,
348 which would require a three-phase model, not within the scope here. Therefore, entrained ice is consid-
349 ered viscous fluid from the beginning. A physically better founded representation of the initial phase of
350 the event would require an extension of the flow model employed. Such an extension could build on the
351 rock-ice avalanche model introduced by Pudasaini and Krautblatter (2014). Also the vertical patterns of
352 the situation illustrated in Fig. 5 cannot be modelled with the present approach, which (i) does not con-
353 sider melting of ice; and (ii) only allows one entrainable layer at each pixel. The assumption of fluid be-
354 haviour of glacier ice therefore represents a necessary simplification which is supported by observations
355 (Fig. 3b), but neglects the likely presence of remaining ice in the basal part of the eroded glacier, which
356 melted later and so contributed to the successive debris flow surges.

357 Still, we currently consider the Pudasaini (2012) model – and the extended multi-phase model (Puda-
358 saini and Mergili, 2019) – best practice, even though other two-phase or bulk mixture models do exist.
359 Most recently, Iverson and George (2014) presented an approach that has been solved with an open
360 source software, called D-Claw (George and Iverson, 2014), and compared to large-scale experiments
361 considering dense debris materials (Iverson et al., 2000; Iverson et al., 2010). The Iverson and George
362 (2014) model can be useful for very dense debris flows where the solid particles and fluid molecules
363 move together. However, its applicability to cascading mass flows is limited for the following reasons: (i)
364 this model assumes that the solid and fluid velocities are the same, an assumption that does not hold for
365 complex, cascading mass flows; (ii) the pore fluid pressure evolution equation includes pore pressure
366 advection and source terms associated with dilation, but ignores the pore fluid diffusion; (iii) there are
367 no real interfacial momentum transfers, such as the drag force, virtual mass force, and buoyancy be-
368 tween the solid and fluid phases; and (iv) neither viscous shear stress, nor dynamical coupling between
369 the pore fluid pressure evolution and the bulk momentum equations are considered. Furthermore, as the
370 fluid pressure evolution is assumed to play a substantial role in the Iverson and George (2014) model, the
371 solid and fluid dynamics cannot be similar, and thus the assumption of negligible relative velocity be-
372 tween solid and fluid is questionable (Pitman and Le, 2005; Pudasaini, 2012).

373 The initial rock slide-rock fall and the rock avalanche are simulated in a plausible way, at least with re-
374 gard to the deposition area. Whereas the simulated deposition area is clearly defined in Scenario S2, this
375 is to a lesser extent the case in Scenario S1, where the front of the rock avalanche directly transforms
376 into a debris flow. Both scenarios seem to overestimate the time between release and deposition, com-

pared to the seismic signals recorded – an issue also reported by WSL (2017) for their simulation. We observe a relatively gradual deceleration of the simulated avalanche, without clearly defined stopping and note that also in the Scenario S2, there is some diffusion after the considered time of 120 s, so that the definition of the simulated deposit is somehow arbitrary. The elaboration of well-suited stopping criteria, going beyond the very simple approach introduced by Mergili et al. (2017), remains a task for the future. However, as the rock avalanche has already been successfully back-calculated by WSL (2017), we focus on the first debris flow surge: the simulation input is optimized towards the back-calculation of the debris flow volumes entering the valley at the hydrograph profile O2 (Table 3). The travel times to the hydrograph profiles O3 and O4 are reproduced in a plausible way in both scenarios, and so are the impact areas (Figs. 8 and 11). Exceedance of the lateral limits in the lower zones is attributed to an overestimate of the debris flow volumes there, and to numerical issues related to the narrow gorge. The same is true for the fan of Bondo. The solid ratio of the debris flow in the simulations appears realistic, ranging around 40–45% in the early stage of the debris flow, and around 30–35% and lower (depending on the cut-off time of the hydrograph) in the final stage. This means that solid material tends to stop in the transit area rather than fluid material, as it can be expected. Nevertheless, the correct simulation of the deposition of debris flow material along Val Bondasca remains a major challenge (Table 3). Even though a considerable amount of effort was put in reproducing the much lower volumes reported in the vicinity of O4, the simulations result in an overestimate of the volumes passing through this hydrograph profile. This is most likely a consequence of the failure of r.avaflow to adequately reproduce the deposition pattern in the zones D and E. Whereas some material remains there at the end of the simulation, more work is necessary to appropriately understand the mechanisms of deposition in viscous debris flows (Pudasaini and Fischer, 2016b). Part of the discrepancy, however, might be explained by the fact that part of the fluid material – which does not only consist of pure water, but of a mixture of water and fine mud – left the area of interest in downstream direction and was therefore not included in the reference measurements.

The simulation results are strongly influenced by the initial conditions and the model parameters. Parameterization of both scenarios is complex and highly uncertain, particularly in terms of optimizing the volumes of entrained till and glacial meltwater, and injected pore water. In general, the parameter sets optimized to yield empirically adequate results are physically plausible, in contrast to Mergili et al. (2018b) who had to set the basal friction angle in a certain zone to a negligible value in order to reproduce the observed overtopping of a more than 100 m high ridge (1970 Huascarán landslide). In contrast, reproducing the travel times to O4 in the present study requires the assumption of a low mobility of the flow in Zone E. This is achieved by increasing the friction (Table 1), accounting for the narrow flow

410 channel, i.e. the interaction of the flow with the channel walls, which is not directly accounted for in
411 r.avaflow. Still, the high values of δ given in Table 1 are not directly applied, as they scale with the solid
412 fraction. This type of weighting has to be further scrutinized. We emphasize that also reasonable param-
413 eter sets are not necessarily physically true, as the large number of parameters involved (Tables 1 and 2)
414 creates a lot of space for equifinality issues (Beven et al., 1996).

415 We have further shown that the classical evaluation of empirical adequacy, by comparing observed and
416 simulated impact areas, is not enough in the case of complex mass flows: travel times, hydrographs, and
417 volumes involved can provide important insight in addition to the classical quantitative performance
418 indicators used, for example, in landslide susceptibility modelling (Formetta et al., 2015). Further, the
419 delineation of the observed impact area is uncertain as the boundary of the event is not clearly defined
420 particularly in Zone C.

421 The present work is seen as a further step towards a better understanding of the challenges and the pa-
422 rameterization concerning the integrated simulation of complex mass flows. More case studies are neces-
423 sary to derive guiding parameter sets facilitating predictive simulations of such events (Mergili et al.,
424 2018a, b). A particular challenge of such case studies consists in the parameter optimization procedure:
425 in principle, automated methods do exist (e.g. Fischer, 2013). However, they have been developed for
426 optimizing globally defined parameters (which are constant over the entire study area) against runout
427 length and impact area, and such tools do a very good job for exactly this purpose. However, they cannot
428 directly deal with spatially variable parameters, as they are defined in the present work. With some
429 modifications they might even serve for that – but the main issue is that optimization also considers
430 shapes and maximum values of hydrograph discharges, or travel times at different places of the path. It
431 would be a huge effort to trim optimization algorithms to this purpose, and to make them efficient
432 enough to prevent excessive computational times – we consider this as an important task for the future
433 which is out of scope of the present work. Therefore, we have used a step-wise expert-based optimiza-
434 tion strategy.

435 7 Conclusions

436 Both of the investigated Scenarios S1 (debris flow developing at the front of the rock avalanche) and S2
437 (debris flow developing at the back of the rock avalanche, overtopping the deposit) lead to empirically
438 reasonably adequate results, when back calculated with r.avaflow using physically plausible model pa-
439 rameters. Based on the simulations performed in the present study, final conclusions on the more likely
440 of the mechanisms sketched in Fig. 6 can therefore not be drawn purely based on the simulations. The

441 observed jet of glacial meltwater (Fig. 3b) points towards Scenario S1. The observed scouring of the rock
442 avalanche deposit, in contrast, rather points towards Scenario S2, but could also be associated to subse-
443 quent debris flow surges. Open questions include at least (i) the interaction between the initial rock
444 slide-rock fall and the glacier; (ii) flow transformations in the lower portion of Zone C (Fig. 7), leading to
445 the first debris flow surge; and (iii) the mechanisms of deposition of 90% of the debris flow material
446 along the flow channel in the Val Bondasca. Further research is therefore urgently needed to shed more
447 light on this extraordinary landslide cascade in the Swiss Alps. In addition, improved simulation con-
448 cepts are needed to better capture the dynamics of complex landslides in glacierized environments: such
449 would particularly have to include three-phase models, where ice – and melting of ice – are considered
450 in a more explicit way. Finally, more case studies of complex mass flows have to be performed in order
451 to derive guiding parameter sets serving for predictive simulations.

452 **Code availability**

453 The r.avaflow code, including a detailed manual, is available for download at the r.avaflow website
454 (Mergili and Pudasaini, 2019).

455 **Data availability**

456 The study is largely based on the 2011 swisstopo MNS-Digital Elevation Model (DEM) (contract: swis-
457 stopo–DV084371), and derivatives thereof. Unfortunately, the authors are not entitled to make these
458 data publicly available.

459

460 **Author contributions**

461 Martin Mergili (MM), Michel Jaboyedoff (MJ), José Pullarello (JP), Shiva P. Pudasaini (SP)
462 MM has contributed to the conceptualization and methodology of the research, designed the software,
463 and performed the formal analysis, visualization, validation, and most of the writing of the original draft.
464 MJ was involved in the conceptualization, investigation, and supervision as well as in the review and
465 editing of the manuscript. JP has contributed to the investigation, visualization, and review & editing. SP
466 has provided input in terms of methodology and review & editing of the manuscript.

467 Competing interests

468 The authors declare that they have no conflict of interest.

469 Acknowledgements

470 Shiva P. Pudasaini gratefully thanks the Herbette Foundation for providing financial support for his sab-
471 batical visit to the University of Lausanne, Switzerland in the period April–June 2018, where this con-
472 tribution was triggered. Similarly, this work has been financially supported by the German Research
473 Foundation (DFG) through the research project PU 386/5-1: “A novel and unified solution to multi-
474 phase mass flows”. It strongly builds on the outcomes of the international cooperation project “A GIS
475 simulation model for avalanche and debris flows (avaflow)” supported by the German Research Founda-
476 tion (DFG, project number PU 386/3-1) and the Austrian Science Fund (FWF, project number I 1600-
477 N30).

478 We would like to thank Brian McArdell and another anonymous reviewer for providing constructive
479 comments and suggestions that helped to enhance the paper substantially, and are grateful to Sophia
480 Demmel and Florian Amann for valuable discussions and to Matthias Benedikt for comprehensive tech-
481 nical assistance.

482 References

483 Amann, F., Kos, A., Phillips, M., and Kenner, R.: The Piz Cengalo Bergsturz and subsequent debris flows,
484 Geophys. Res. Abstr., 20, 14700, 2018.

485 Amt für Wald und Naturgefahren: Bondo: Chronologie der Ereignisse, 2 pp.,
486 [https://www.gr.ch/DE/institutionen/verwaltung/bvfd/awn/dokumentenliste_afw/20170828_Chronologie
487 _Bondo_2017_12_13_dt.pdf](https://www.gr.ch/DE/institutionen/verwaltung/bvfd/awn/dokumentenliste_afw/20170828_Chronologie_Bondo_2017_12_13_dt.pdf), accessed on 31 May 2019.

488 Beven, K.: Equifinality and Uncertainty in Geomorphological Modelling, in: The Scientific Nature of
489 Geomorphology: Proceedings of the 27th Binghamton Symposium in Geomorphology, 27-29 September
490 1996, John Wiley & Sons, 289–313, 1996.

491 Bonanomi, Y., and Keiser, M.: Bericht zum aktuellen Bergsturz am Piz Cengalo 2017, Bergeller Alpen im
492 Engadin, 19. Geoforum Umhausen, 19.–20. Oktober 2017, 55–60, 2017.

493 Christen, M., Kowalski, J., and Bartelt, P.: RAMMS: Numerical simulation of dense snow avalanches in
494 three-dimensional terrain, Cold Reg. Sci. Technol., 63, 1–14,
495 <https://doi.org/10.1016/j.coldregions.2010.04.005>, 2010.

496 De Blasio, F. V., and Crosta, G. B.: Extremely Energetic Rockfalls: Some preliminary estimates, in: Land-
497 slides and Engineered Slopes. Experience, Theory and Practice, 759–764, CRC Press, 2016.

498 Demmel, S.: Water Balance in Val Bondasca. Initial hydrological conditions for debris flows triggered by
499 the 2017 rock avalanche at Pizzo Cengalo. Master Thesis, ETH Zurich, 50 pp., 2019.

500 Domnik, B., Pudasaini, S. P., Katzenbach, R., and Miller, S. A.: Coupling of full two-dimensional and
501 depth-averaged models for granular flows, *J. Non-Newtonian Fluid Mech.*, 201, 56–68,
502 <https://doi.org/10.1016/j.jnnfm.2013.07.005>, 2013.

503 Evans, S. G., Bishop, N.F., Fidel Smoll, L., Valderrama Murillo, P., Delaney, K.B., and Oliver-Smith, A.:
504 A re-examination of the mechanism and human impact of catastrophic mass flows originating on Neva-
505 do Huascarán, Cordillera Blanca, Peru in 1962 and 1970, *Eng. Geol.*, 108, 96–118,
506 <https://doi.org/10.1016/j.enggeo.2009.06.020>, 2009.

507 Fischer, J.-T., Kowalski, J., and Pudasaini, S. P.: Topographic curvature effects in applied avalanche mod-
508 eling, *Cold Reg. Sci. Technol.*, 74, 21–30, <https://doi.org/10.1016/j.coldregions.2012.01.005>, 2012.

509 Fischer, J.-T., Kofler, A., Fellin, W., Granig, M., and Kleemayr, K.: Multivariate parameter optimization
510 for computational snow avalanche simulation in 3d terrain, *J. Glaciol.*, 61(229), 875–888,
511 <https://doi.org/10.3189/2015JoG14J168>, 2015.

512 Formetta, G., Capparelli, G., and Versace, P.: Evaluating performances of simplified physically based
513 models for landslide susceptibility, *Hydrol. Earth Syst. Sci. Discuss.*, 12, 13217–13256,
514 <https://doi.org/10.5194/hessd-19-1-2015>, 2015.

515 Frank, F., Huggel, C., McArdell, B. W., and Vieli, A.: Landslides and increased debris-flow activity: a
516 systematic comparison of six catchments in Switzerland. *Earth Surf. Proc. Landforms*, 44(3), 699–712,
517 <https://doi.org/10.1002/esp.4524>, 2019.

518 George, D. L., and Iverson, R. M.: A depth-averaged debris-flow model that includes the effects of evolv-
519 ing dilatancy. II. Numerical predictions and experimental tests. *Proc. Royal Soc. A*, 470(2170), 20130820,
520 <https://doi.org/10.1098/rspa.2013.0820>, 2014.

521 Haeberli, W.: Mountain permafrost—research frontiers and a special long-term challenge, *Cold Reg. Sci.*
522 *Technol.*, 96, 71–76, <https://doi.org/10.1016/j.coldregions.2013.02.004>, 2013.

523 Haeberli, W., and Whiteman, C. (Eds.): *Snow and Ice-related Hazards, Risks and Disasters*, Elsevier,
524 <https://doi.org/10.1016/B978-0-12-394849-6.00001-9>, 2014.

525 Haeberli, W., Schaub, Y., and Huggel, C.: Increasing risks related to landslides from degrading perma-
526 frost into new lakes in de-glaciating mountain ranges, *Geomorphology*, 293(B), 405–417,
527 <https://doi.org/10.1016/j.geomorph.2016.02.009>, 2017.

528 Harris, C., Arenson, L. U., Christiansen, H. H., Etzelmüller, B., Frauenfelder, R., Gruber, S., Haeberli,
529 W., Hauck., C., Hözle, M., Humlum, O., Isaksen, K., Kääb, A., Kern-Lütschg, M. A., Lehning, M., Mat-
530 suoka, N., Murton, J. B., Nötzli, J., Phillips, M., Ross, N., Seppälä, M., Springman, S. M., and Vonder
531 Mühl, D.: Permafrost and climate in Europe: Monitoring and modelling thermal, geomorphological and
532 geotechnical responses, *Earth-Sci. Rev.*, 92, 117–171, <https://doi.org/10.1016/j.earscirev.2008.12.002>,
533 2009.

534 Hewitt, K.: Styles of rock-avalanche depositional complexes conditioned by very rugged terrain, Karako-
535 ram Himalaya, *Pakistan, Rev. Eng. Geol.*, 15, 345–377, 2002.

536 Huggel, C., Zgraggen-Oswald, S., Haeberli, W., Kääb, A., Polkvoj, A., Galushkin, I., and Evans, S.G.: The
537 2002 rock/ice avalanche at Kolka/Karmadon, Russian Caucasus: assessment of extraordinary avalanche
538 formation and mobility, and application of QuickBird satellite imagery, *Nat. Hazards Earth Syst. Sci.*, 5,
539 173–187, <https://doi.org/10.5194/nhess-5-173-2005>, 2005.

540 Iverson, R. M.: The physics of debris flows, *Rev. Geophys.*, 35, 245–296,
541 <https://doi.org/10.1029/97RG00426>, 1997.

542 Iverson, R. M., Reid, M. E., Iverson, N. R., LaHusen, R. G., Logan, M., Mann, J. E., and Brien, D. L.:
543 Acute sensitivity of landslide rates to initial soil porosity, *Science*, 290, 513–516,
544 <https://doi.org/10.1126/science.290.5491.513>, 2000.

545 Iverson, R. M., Logan, M., LaHusen, R. G., and Berti, M.: The perfect debris flow? aggregated results
546 from 28 large-scale experiments, *J. Geophys. Res.*, 115, 1-29, <https://doi.org/10.1029/2009JF001514>, 2010.

547 Iverson, R. M., and George, D. L.: A depth-averaged debris-flow model that includes the effects of evolv-
548 ing dilatancy. I. Physical basis, *Proc. Royal Soc. A*, 470(2170), 20130819,
549 <https://doi.org/10.1098/rspa.2013.0819>, 2014.

550 Kattel. P , Khattri, K. B., Pokhrel, P. R., Kafle, J., Tuladhar, B. M., and Pudasaini, S. P.: Simulating glacial
551 lake outburst floods with a two-phase mass flow model, *Ann. Glaciol.*, 57(71), 349–358,
552 <https://doi.org/10.3189/2016AoG71A039>, 2016.

553 Krautblatter, M., Funk, D., and Günzel, F. K.: Why permafrost rocks become unstable: a rock–ice-
554 mechanical model in time and space, *Earth Surf. Process. Landf.*, 38, 876–887,
555 <https://doi.org/10.1002/esp.3374>, 2013.

556 McDougall, S., and Hungr, O.: A Model for the Analysis of Rapid Landslide Motion across Three-
557 Dimensional Terrain, *Can. Geotech. J.*, 41, 1084–1097, <https://doi.org/10.1139/t04-052>, 2004.

558 Mergili, M., Pudasaini, S. P.: r.avaflow – The open source mass flow simulation model,
559 <https://www.avaflow.org/>, last access: 7 July 2019.

560 Mergili, M., Fischer, J.-T., Krenn, J., and Pudasaini, S. P.: r.avaflow v1, an advanced open source compu-
561 tational framework for the propagation and interaction of two-phase mass flows, *Geosci. Model Dev.*, 10,
562 553–569, <https://doi.org/10.5194/gmd-10-553-2017>, 2017.

563 Mergili, M., Emmer, A., Juřicová, A., Cochachin, A., Fischer, J.-T., Huggel, C., and Pudasaini, S.P.: How
564 well can we simulate complex hydro-geomorphic process chains? The 2012 multi-lake outburst flood in
565 the Santa Cruz Valley (Cordillera Blanca, Perú), *Earth Surf. Process. Landf.*, 43(7), 1373–1389,
566 <https://doi.org/10.1002/esp.4318>, 2018a.

567 Mergili, M., Frank, B., Fischer, J.-T., Huggel, C., and Pudasaini, S. P.: Computational experiments on the
568 1962 and 1970 landslide events at Huascarán (Peru) with r.avaflow: Lessons learned for predictive mass
569 flow simulations, *Geomorphology*, 322, 15–28, <https://doi.org/10.1016/j.geomorph.2018.08.032>, 2018b.

570 Nessimyahu, H., and Tadmor, E.: Non-oscillatory central differencing for hyperbolic conservation laws, *J.*
571 *Comput. Phys.*, 87, 408–463, [https://doi.org/10.1016/0021-9991\(90\)90260-8](https://doi.org/10.1016/0021-9991(90)90260-8), 1990.

572 Nicoletti, G. P., and Sorriso-Valvo, M.: Geomorphic controls of the shape and mobility of rock ava-
573 lanches, *GSA Bull.*, 103(10), 1365–1373, [https://doi.org/10.1130/0016-
574 7606\(1991\)103<1365:GCOTSA>2.3.CO;2](https://doi.org/10.1130/0016-7606(1991)103<1365:GCOTSA>2.3.CO;2), 1991.

575 Pitman, E.B., and Le, L.: A two-fluid model for avalanche and debris flows. *Philos. Trans. R. Soc. A*, 363,
576 1573–1601, <https://doi.org/10.1098/rsta.2005.1596>, 2005.

577 Pudasaini, S. P.: A general two-phase debris flow model, *J. Geophys. Res. Earth Surf.*, 117, F03010,
578 <https://doi.org/10.1029/2011JF002186>, 2012.

579 Pudasaini, S. P.: A full description of generalized drag in mixture mass flows, *Phys. Fluids*, submitted
580 manuscript, 2019.

581 Pudasaini, S. P., and Krautblatter, M.: A two-phase mechanical model for rock-ice avalanches, *J. Ge-
582 ophys. Res. Earth Surf.*, 119, doi:10.1002/2014JF003183, 2014.

583 Pudasaini, S. P., and Fischer, J.-T.: A mechanical model for phase-separation in debris flow,
584 arXiv:1610.03649, 2016a.

585 Pudasaini, S.P., and Fischer, J.-T.: A mechanical erosion model for two-phase mass flows,
586 arXiv:1610.01806, 2016b.

587 Pudasaini, S.P., and Mergili, M.: A Multi-Phase Mass Flow Model, *J. Geophys. Res. Earth Surf.*,
588 JGRF21102, <https://doi.org/10.1029/2019JF005204>, 2019.

589 Preh, A., and Sausgruber, J. T.: The Extraordinary Rock-Snow Avalanche of Alpl, Tyrol, Austria. Is it
590 Possible to Predict the Runout by Means of Single-phase Voellmy- or Coulomb-Type Models?, in: Engi-
591 neering Geology for Society and Territory–Volume 2, edited by: Lollino, G. et al., Springer, Cham,
592 https://doi.org/10.1007/978-3-319-09057-3_338, 2015.

593 Saltelli, A., and Annoni, P.: How to avoid a perfunctory sensitivity analysis, *Environ. Model. Softw.*, 25,
594 1508–1517, <https://doi.org/10.1016/j.envsoft.2010.04.012>, 2010.

595 Savage, S. B., and Hutter, K.: The motion of a finite mass of granular material down a rough incline, *J.*
596 *Fluid Mech.*, 199, 177–215, <https://doi.org/10.1017/S0022112089000340>, 1989.

597 Scheidegger, A. E.: On the Prediction of the Reach and Velocity of Catastrophic Landslides, *Rock Mech.*,
598 5, 231–236, <https://doi.org/10.1007/BF01301796>, 1973.

599 Schneider, D., Huggel, C., Cochachin, A., Guillén, S., and García, J.: Mapping hazards from glacier lake
600 outburst floods based on modelling of process cascades at Lake 513, Carhuaz, Peru, *Adv. Geosci.*, 35,
601 145–155, <https://doi.org/10.5194/adgeo-35-145-2014>, 2014.

602 Somos-Valenzuela, M. A., Chisolm, R. E., Rivas, D. S., Portocarrero, C., and McKinney, D. C.: Modeling
603 a glacial lake outburst flood process chain: the case of Lake Palcacocha and Huaraz, Peru, *Hydrol. Earth
604 Syst. Sci.*, 20, 2519–2543, <https://doi.org/10.5194/hess-20-2519-2016>, 2016.

605 Steinacher, R., Kuster, C., Buchli, C., and Meier, L.: The Pizzo Cengalo and Val Bondasca events: From
606 early warnings to immediate alarms, *Geophys. Res. Abstr.* 20, 17536, 2018.

607 Tai, Y. C., Noelle, S., Gray, J. M. N. T., and Hutter, K.: Shock-capturing and front-tracking methods for
608 granular avalanches, *J. Comput. Phys.*, 175(1), 269–301, <https://doi.org/10.1006/jcph.2001.6946>, 2002.

609 VAW: Vadrec dal Cengal Ost: Veränderungen in Vergangenheit und Zukunft. Laboratory of Hydraulics,
610 Hydrology and Glaciology of the Swiss Federal Institute of Technology Zurich, 17 pp.,
611 [https://www.gr.ch/DE/institutionen/verwaltung/bvfd/awn/dokumentenliste_afw/Cengalo%20Gletschere
ntwicklung%20ETH_2nov_final.pdf](https://www.gr.ch/DE/institutionen/verwaltung/bvfd/awn/dokumentenliste_afw/Cengalo%20Gletschere
612 ntwicklung%20ETH_2nov_final.pdf), accessed on 31 May 2019, 2017.

613 Voellmy, A.: Über die Zerstörungskraft von Lawinen, *Schweizerische Bauzeitung*, 73, 159–162, 212–217,
614 246–249, 280–285, 1955.

615 Walter, F., Wenner, M., and Amann, F.: Seismic Analysis of the August 2017 Landslide on Piz Cengalo
616 (Switzerland), *Geophys. Res. Abstr.*, 20, 3163-1, 2018.

617 Walter, F., Amann, F., Kos, A., Kenner, R., Phillips, M., de Preux, A., Huss, M., Tognacca, C., Clinton, J.,
618 Diehl, T., and Bonanomi, Y.: Direct observations of a three million cubic meter rock-slope collapse with
619 almost immediate initiation of ensuing debris flows, *Earth Planet. Sci. Lett.*, submitted manuscript, 2019.

620 Wang, Y., Hutter, K., and Pudasaini, S. P.: The Savage-Hutter theory: A system of partial differential
621 equations for avalanche flows of snow, debris, and mud, *ZAMM – J. Appl. Math. Mech.*, 84(8), 507–527,
622 <https://doi.org/10.1002/zamm.200310123>, 2004.

623 Worni, R., Huggel, C., Clague, J. J., Schaub, Y., and Stoffel, M.: Coupling glacial lake impact, dam
624 breach, and flood processes: A modeling perspective, *Geomorphology*, 224, 161–176,
625 <https://doi.org/10.1016/j.geomorph.2014.06.031>, 2014.

626 WSL.: SLF Gutachten G2017.20: Modellierung des Cengalo Bergsturzes mit verschiedenen Rahmenbe-
627 dingungen, Bondo, GR. WSL-Institut für Schnee- und Lawinenforschung SLF, 69 pp.,
628 https://www.gr.ch/DE/institutionen/verwaltung/bvfd/awn/dokumentenliste_afw/SLF_G2017_20_Modell-
629 ierung_Cengalo_Bergsturz_030418_A.pdf, accessed on 31 May 2019, 2017.

630

631 **Tables**

632 Table 1. Descriptions and optimized parameter values for each of the zones A–F (Fig. 4 and Fig. 7). The
 633 names of the model parameters are given in the text and in Table 2. The values provided in Table 2 are
 634 assigned to those parameters not shown. (S1) and (S2) refer to the corresponding scenarios. Explanations
 635 of the superscripts: ¹⁾ Note that in all zones and in both of the scenarios S1 and S2, δ is assumed to scale
 636 linearly with the solid fraction. This means that the values given only apply in case of 100% solid. ²⁾ This
 637 only applies to the initial landslide, which is assumed completely dry in Scenario S2. Due to the scaling
 638 of δ with the solid fraction, a lower basal friction is required to obtain results similar to Scenario S1,
 639 where the rock avalanche contains some fluid. The same values of δ as for Scenario S1 are applied for the
 640 debris flow in Scenario S2 throughout all zones. ³⁾ This volume is derived from our own reconstruction
 641 (Fig. 5). In contrast, WSL (2017) gives 3.1 million m³, and Amann et al. (2018) 3.15 million m³. ⁴⁾ In Sce-
 642 nario S2, the glacier is not directly entrained, but instead released behind the rock avalanche. In both
 643 scenarios, ice is considered to melt immediately on impact and included in the viscous fluid fraction. See
 644 text for more detailed explanations.

Zone	Description	Model parameters	Initial conditions
A	Rock zone – NE face of Piz Cengalo with rock slide-rock fall release area	$\delta = 20^\circ$ (S1) ¹⁾ $\delta = 13^\circ$ (S2) ²⁾ $C_{AD} = 0.2$	Release volume: 3.2 million m ³ , 100 % solid ³⁾
B	Glacier zone – Cirque glacier beneath zone A, entrainment of glacier ice ¹⁾	$\delta = 20^\circ$ (S1) $\delta = 13^\circ$ (S2) $C_E = 10^{-6.5}$	Entrainment of glacier ice and till (Table 3) ⁴⁾
C	Slope zone – steep, partly debris-covered glacier forefield leading down to the Val Bondasca	$\delta = 20^\circ$ (S1) $\delta = 13^\circ$ (S2) $C_E = 10^{-6.5}$ (S1) $C_E = 10^{-8.0}$ (S2)	Entrainment of injected water in Scenario S1 Entrainment of rock avalanche deposit in Scenario S2
D	Upper Val Bondasca zone – clearly defined flow channel becoming narrower in downstream direction	$\delta = 20-45^\circ$	No entrainment allowed, increasing friction
E	Lower Val Bondasca zone – narrow gorge	$\delta = 45^\circ$ $C_{FF} = 0.5$	No entrainment allowed, high friction due to lateral confinement
F	Bondo zone – deposition of the debris flow on the cone of Bondo	$\delta = 20^\circ$	No entrainment allowed

645

646 Table 2. Model parameters used for the simulations. Explanations of the superscripts: ¹⁾ Fluid is here con-
 647 sidered as a mixture of water and fine particles. This explains the higher density, compared to pure wa-
 648 ter. ²⁾ The internal friction angle φ always has to be larger than or equal to the basal friction angle δ .
 649 Therefore, in case of $\delta > \varphi$, φ is increased accordingly.

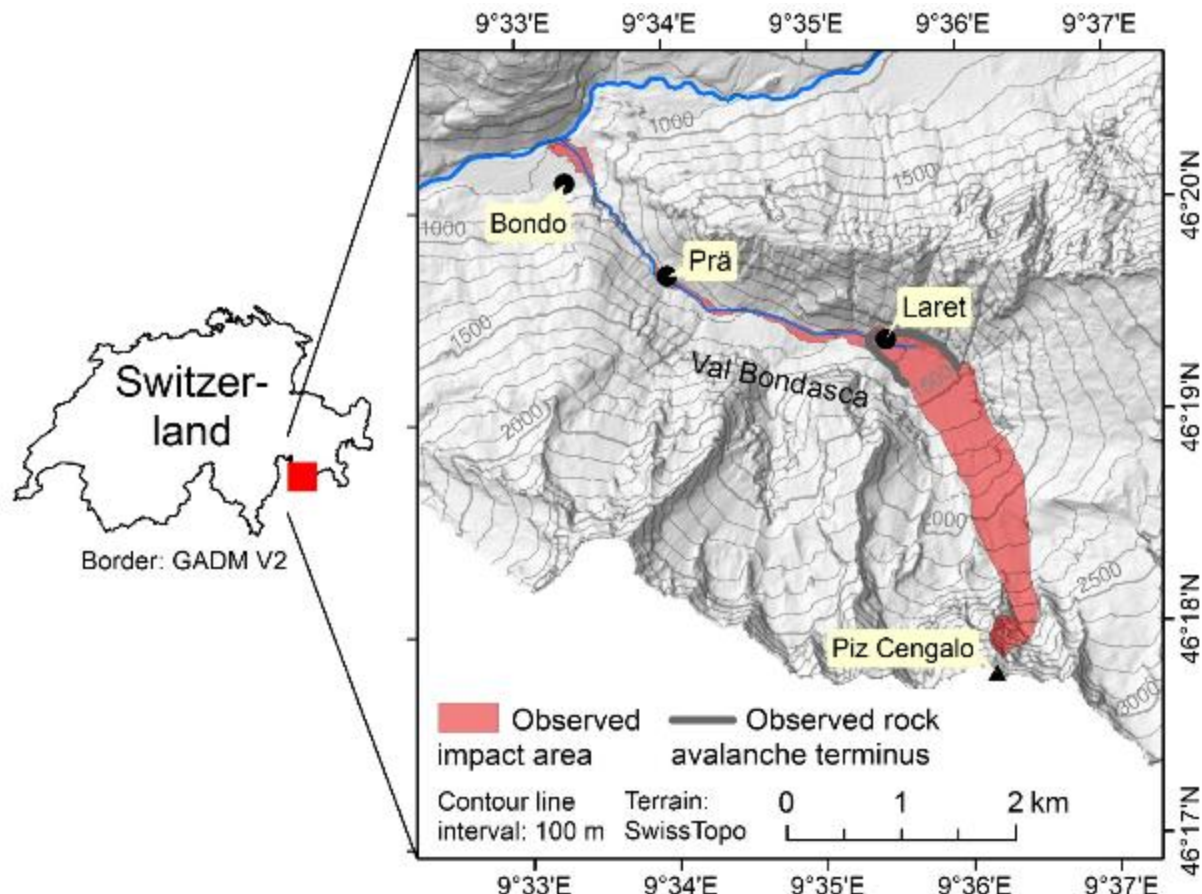
Symbol	Parameter	Unit	Value
ρ_s	Solid material density (grain density)	kg m^{-3}	2,700
ρ_f	Fluid material density	kg m^{-3}	1,400 ¹⁾
φ	Internal friction angle	Degree	27 ²⁾
δ	Basal friction angle	Degree	Table 1
ν	Kinematic viscosity of the fluid	$\text{m}^2 \text{s}^{-1}$	10
τ_y	Yield strength of the fluid	Pa	10
C_{AD}	Ambient drag coefficient	–	0.04 (exceptions in Table 1)
C_{FF}	Fluid friction coefficient	–	0.0 (exceptions in Table 1)
C_E	Entrainment coefficient	–	Table 1

650

651 Table 3. Selected output parameters of the simulations for the Scenarios S1 and S2 compared to the ob-
 652 served or documented parameter values. S = solid; F = fluid; fractions are expressed in terms of volume;
 653 t_0 = time from the initial release to the release of the first debris flow surge. Reference values are extract-
 654 ed from Amt für Wald und Naturgefahren (2017a), Bonanomi and Keiser (2017), and WSL (2017). *** =
 655 empirically adequate (within the documented range of values); ** = empirically partly adequate (less than
 656 50% away from the documented range of values); * = empirically inadequate (at least 50% away from the
 657 documented range of values). The arithmetic means of minimum and maximum of each range are used
 658 for the calculations. Explanations of the superscripts: ¹⁾ Not all the material entrained from the glacier
 659 was relevant for the first debris flow surge (Fig. 6), therefore lower volumes of entrained S (coarse till, in
 660 Scenario S2 also rock avalanche deposit) and F (molten ice and fine till, in Scenario S1 also pore water)
 661 yield the empirically most adequate results. The F volumes originating from the glacier in the simula-
 662 tions represent approx. half of the water equivalent of the entrained ice, corresponding well to the find-
 663 ings of WSL (2017). ²⁾ This value does not include the 145,000 m³ of solid material remobilized through
 664 entrainment from the rock avalanche deposit in Scenario S2. ³⁾ WSL (2017) states that the rock ava-
 665 lanche came to rest approx. 60 s after release, whereas the seismic signals ceased 90 s after release. ⁴⁾ A
 666 certain time (here, we assume a maximum of 30 s) has to be allowed for the initial debris flow surge to
 667 reach O2, located slightly downstream of the front of the rock avalanche deposit. ⁵⁾ WSL (2017) gives a
 668 travel time of 3.5 minutes to Prä, roughly corresponding to the location of O3. It remains unclear
 669 whether this number refers to the release of the initial rock slide-rock fall or (more likely) to the start of
 670 the first debris flow surge. Bonanomi and Keiser (2017) give a travel time of roughly four minutes be-
 671 tween the initial release and the arrival of the first surge at the sensor of Prä. ⁶⁾ Amt für Wald und
 672 Naturgefahren (2017) gives a time span of 17 minutes between the release of the initial rock slide-rock
 673 fall and the arrival of the first debris flow surge at the “bridge” in Bondo. However, it is not indicated to
 674 which bridge this number refers. WSL (2017), in contrast, give a travel time of 7–8 minutes from Prä to
 675 the “old bridge” in Bondo, which, in sum, results in a shorter total travel time as indicated in Amt für
 676 Wald und Naturgefahren (2017). Depending on the bridge, the reference location for these numbers
 677 might be downstream from O4. In the simulation, this hydrograph shows a slow onset – travel times
 678 refer to the point when 5% of the total peak discharge are reached.

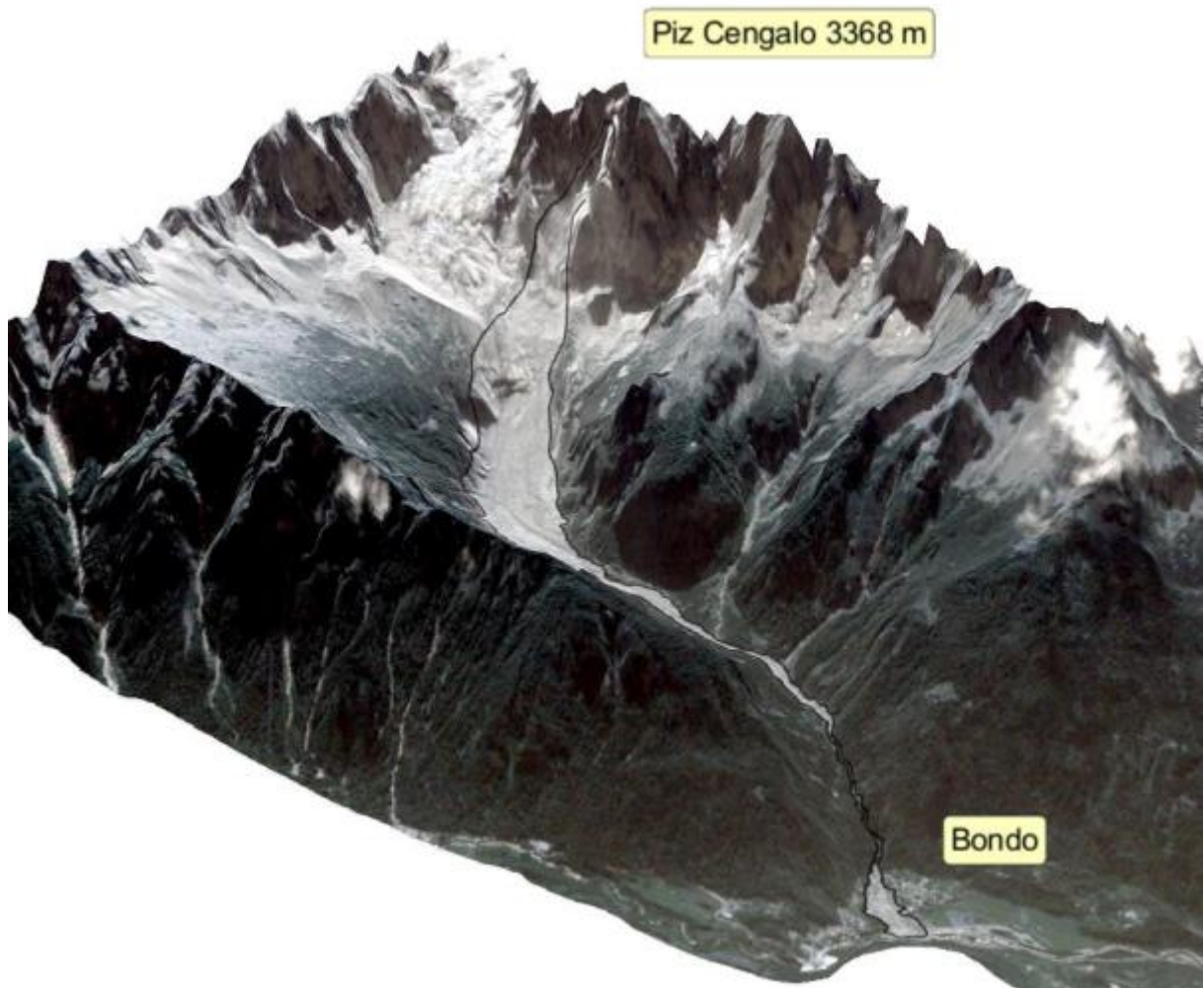
Parameter	Documenta- tion/Observation	Scenario S1	Scenario S2
Entrained ice (m ³)	600,000 ¹⁾	–	–
Entrained S (m ³)	–	60,000	60,000 ²⁾
Entrained F (m ³)	–	305,000	240,000
Duration of initial landslide (s)	60–90 ³⁾	100–120**	100–120**
Travel time to O2 (s)	90–120 ⁴⁾	140**	t_0 +120***
Travel time to O3 (s)	210–300 ⁵⁾	280***	t_0 +240***
Travel time to O4 (s)	630–1020 ⁶⁾	700***	t_0 +640***
Debris flow volume at O2 (m ³)	540,000	530,000** (43% S)	430,000** (45% S)
Debris flow volume at O4 (m ³)	50,000	265,000* (34% S)	270,000* (24% S)

679



681
682 Figure 1. Study area with the impact area of the 2017 Piz Cengalo-Bondo landslide cascade. The ob-
683 served rock avalanche terminus was derived from WSL (2017).

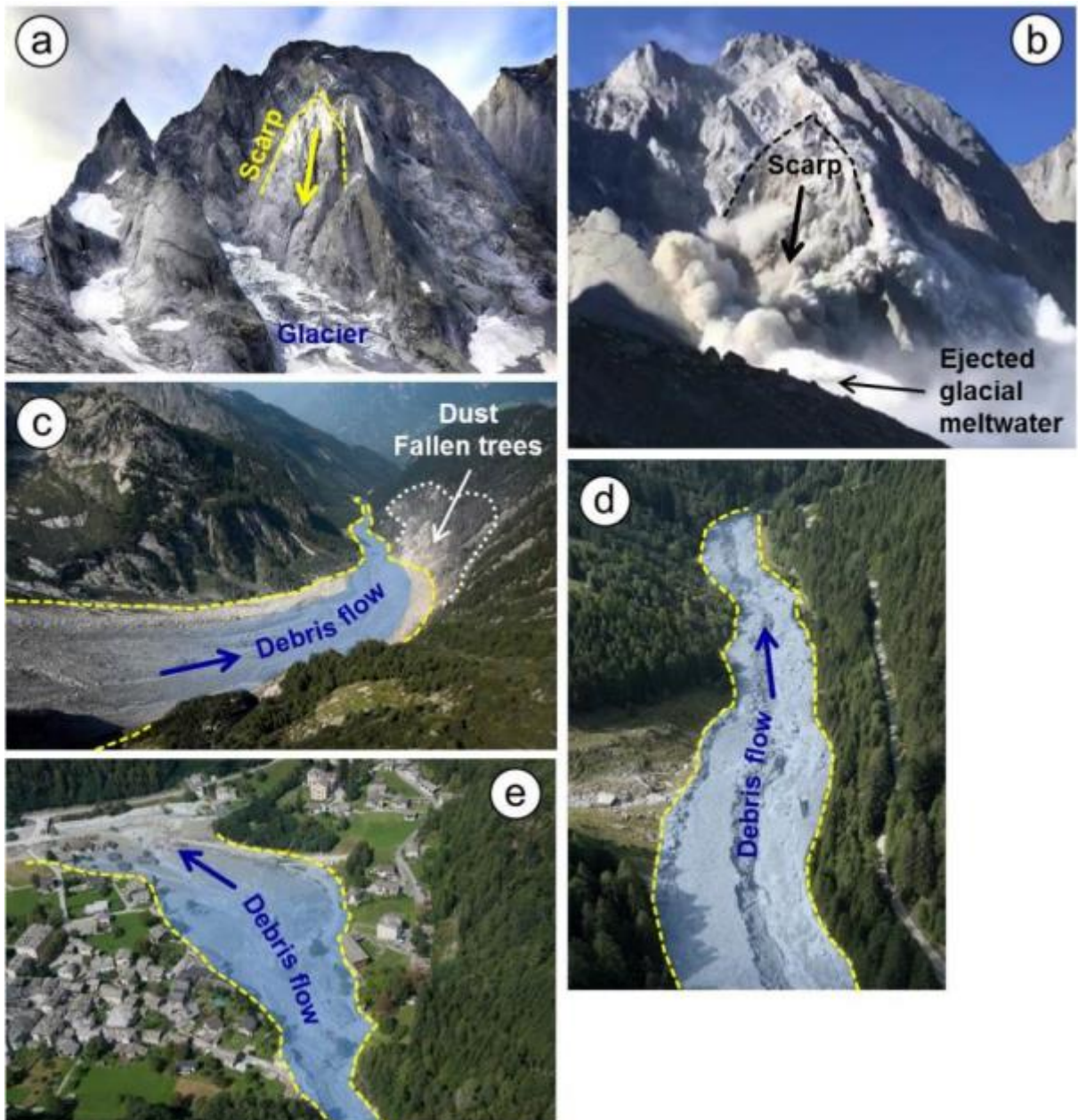
684



685
686
687

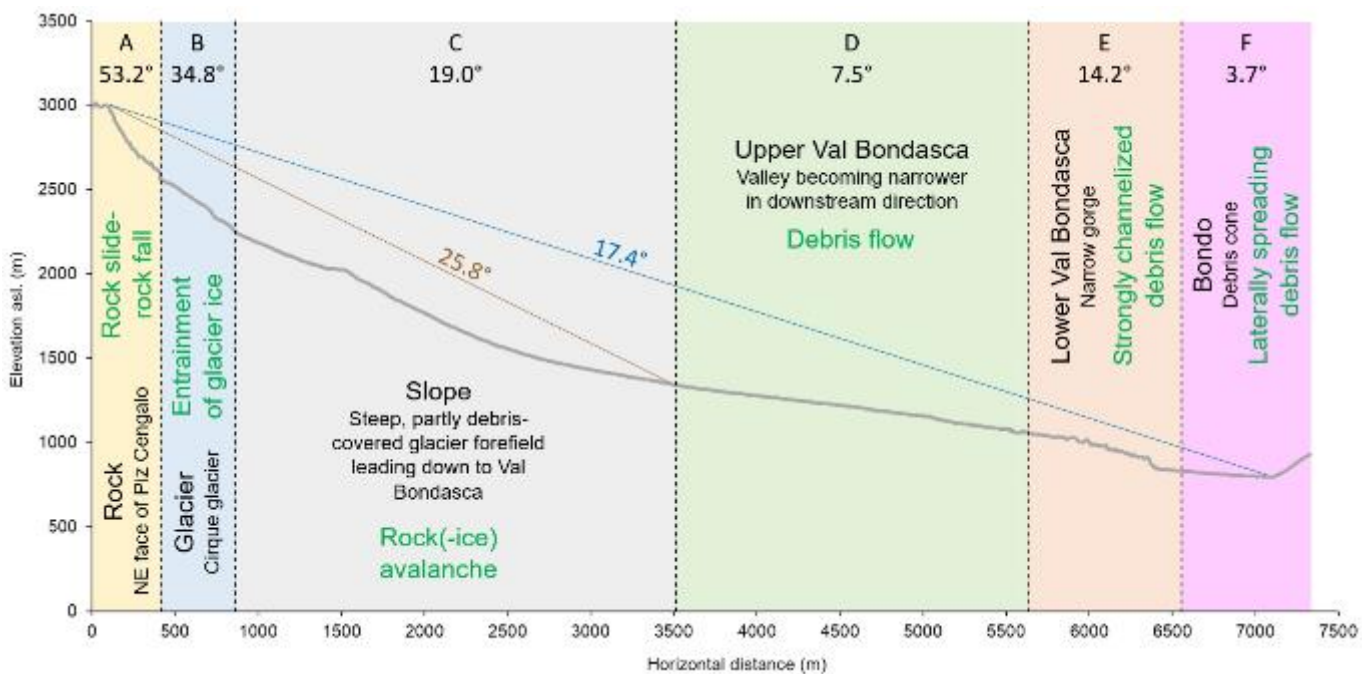
Figure 2. Oblique view of the impact area of the event, orthophoto draped over the 2011 DTM. Data sources: swisstopo.

688



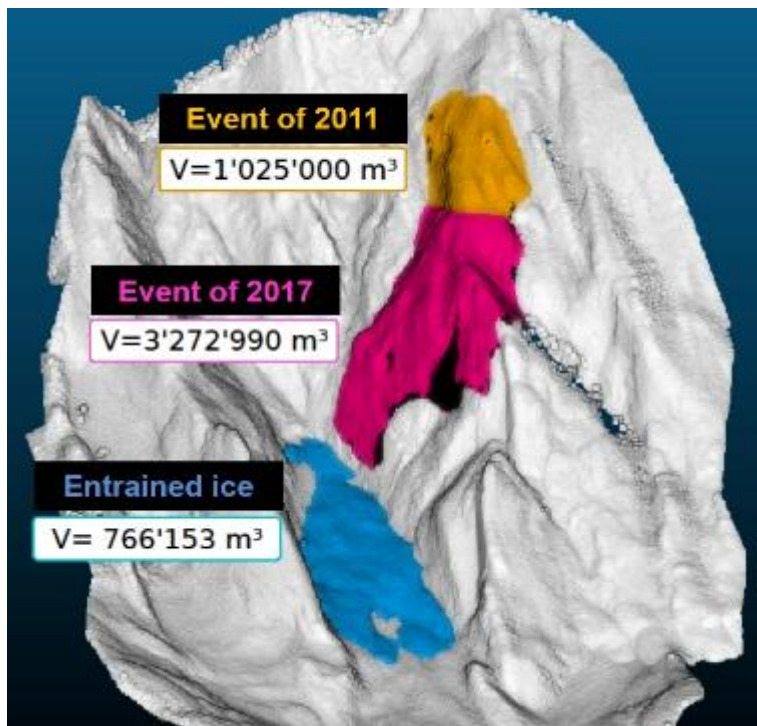
689

690 Figure 3. The 2017 Piz Cengalo-Bondo landslide cascade. (a) Scarp area on 20 September 2014. (b) Scarp
 691 area on 23 September 2017 at 9:30, 20 s after release, frame of a video taken from the Capanna di Sciora.
 692 Note the fountain of water and/or crushed ice at the front of the avalanche, most likely representing
 693 meltwater from the impacted glacier. (c) Upper part of the Val Bondasca, where the channelized debris
 694 flow developed. Note the zone of dust and pressure-induced damages to trees on the right side of the
 695 valley. (d) Traces of the debris flows in the Val Bondasca. (e) The debris cone of Bondo after the event.
 696 Image sources: Daniele Porro (a), Diego Salasc (b), VBS swisstopo Flugdienst (c)–(e).



697
698 Figure 4. Profile along the main flow path of the Piz Cengalo-Bondo landslide cascade. The letters A–F
699 indicate the individual zones (Table 1 and Fig. 7), whereas the associated numbers indicate the average
700 angles of reach along the profile for each zone. The brown number and line show the angle of reach of
701 the initial landslide (rock slide–rock fall and rock(–ice) avalanche), whereas the blue number and line
702 show the angle of reach of the entire landslide cascade. The geomorphic characteristics of the zone (in
703 black) are indicated along with the dominant process type (in green).

704

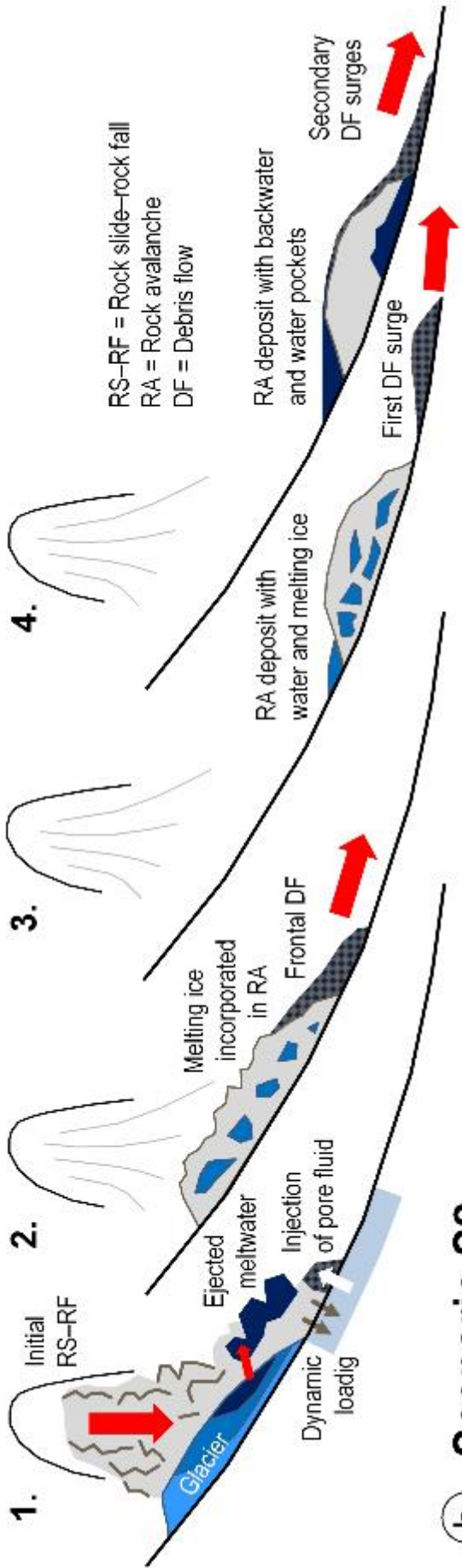


705
706
707
708
709
710

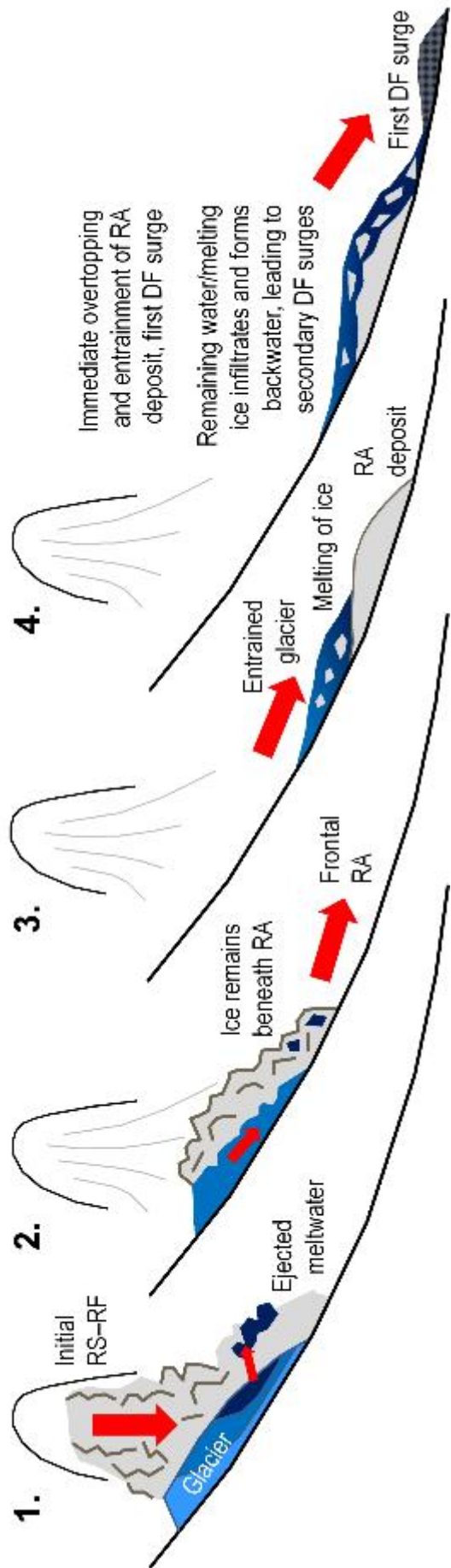
Figure 5. Reconstruction of the released rock volume and the entrained glacier volume in the 2017 Piz Cengalo-Bondo landslide cascade. Note that the boundary between the 2011 and 2017 release volumes is connected to some uncertainties, explaining the slight discrepancies among the reported volumes. The glacier volume shown is neither corrected for entrainment related to the 2011 event, nor for glacier retreat in the period 2011–2017.

711

(a) Scenario S1

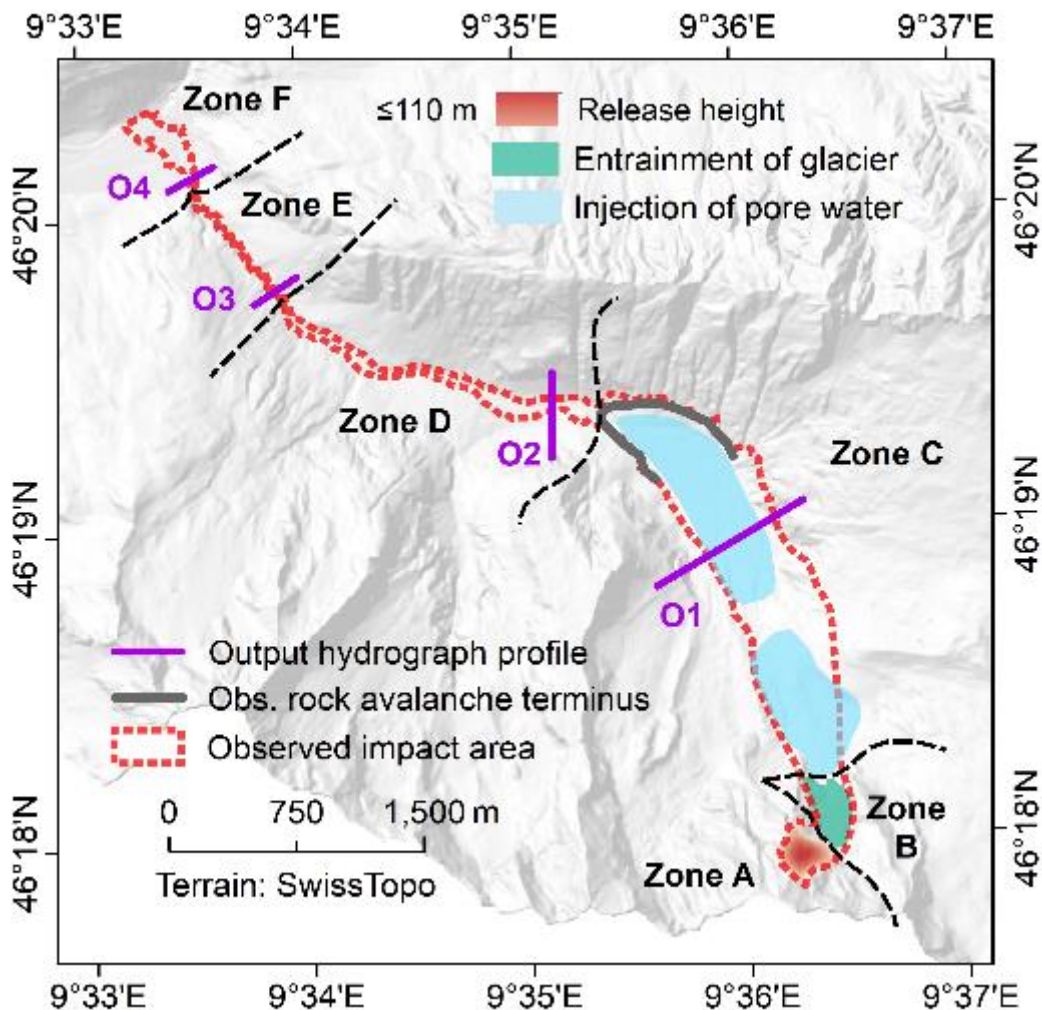


(b) Scenario S2

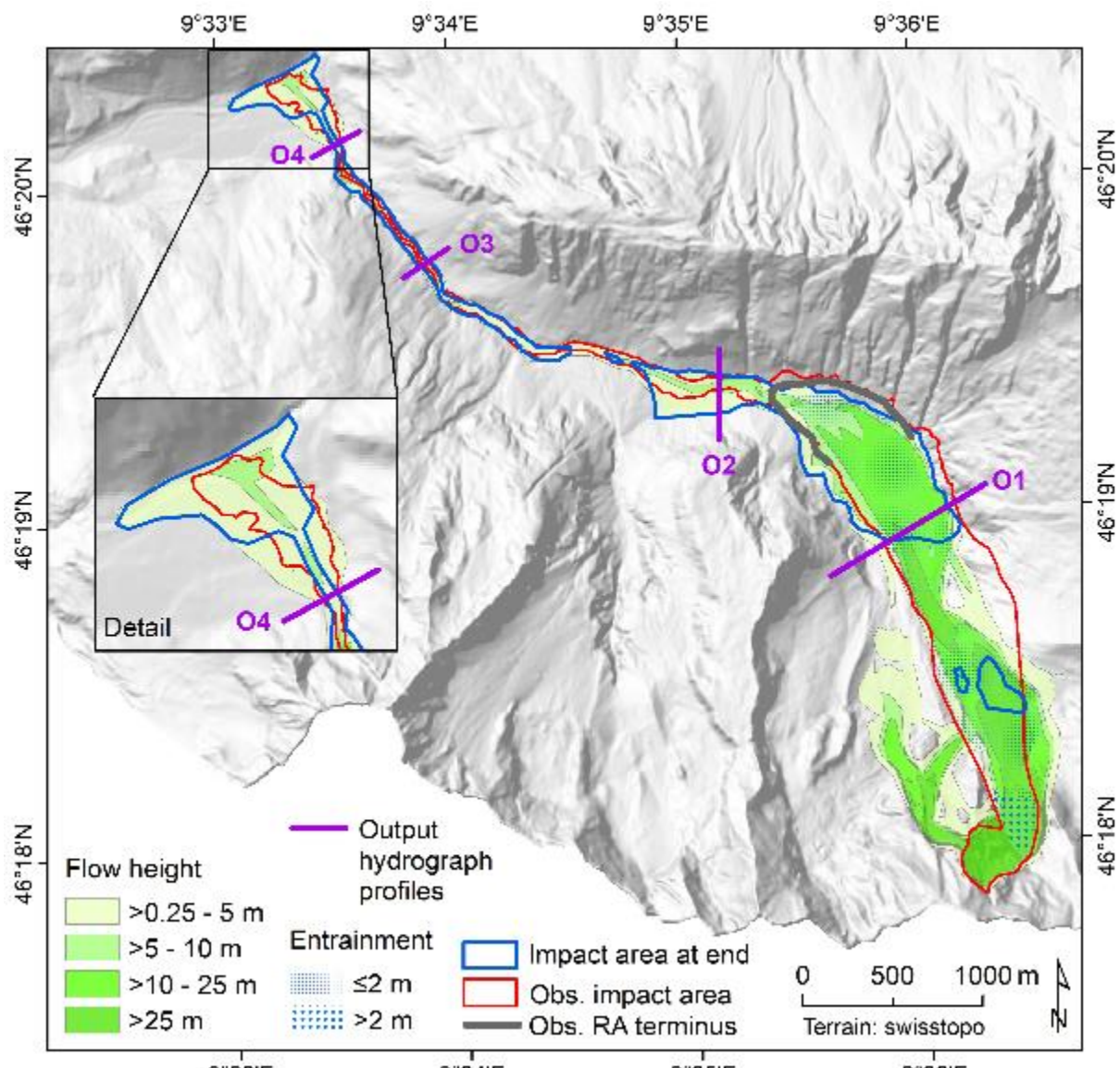


713 Figure 6. Qualitative conceptual models of the rock avalanche-debris flow transformation. (a) Scenario
714 S1; (b) Scenario S2. See text for the detailed description of the two scenarios.

715



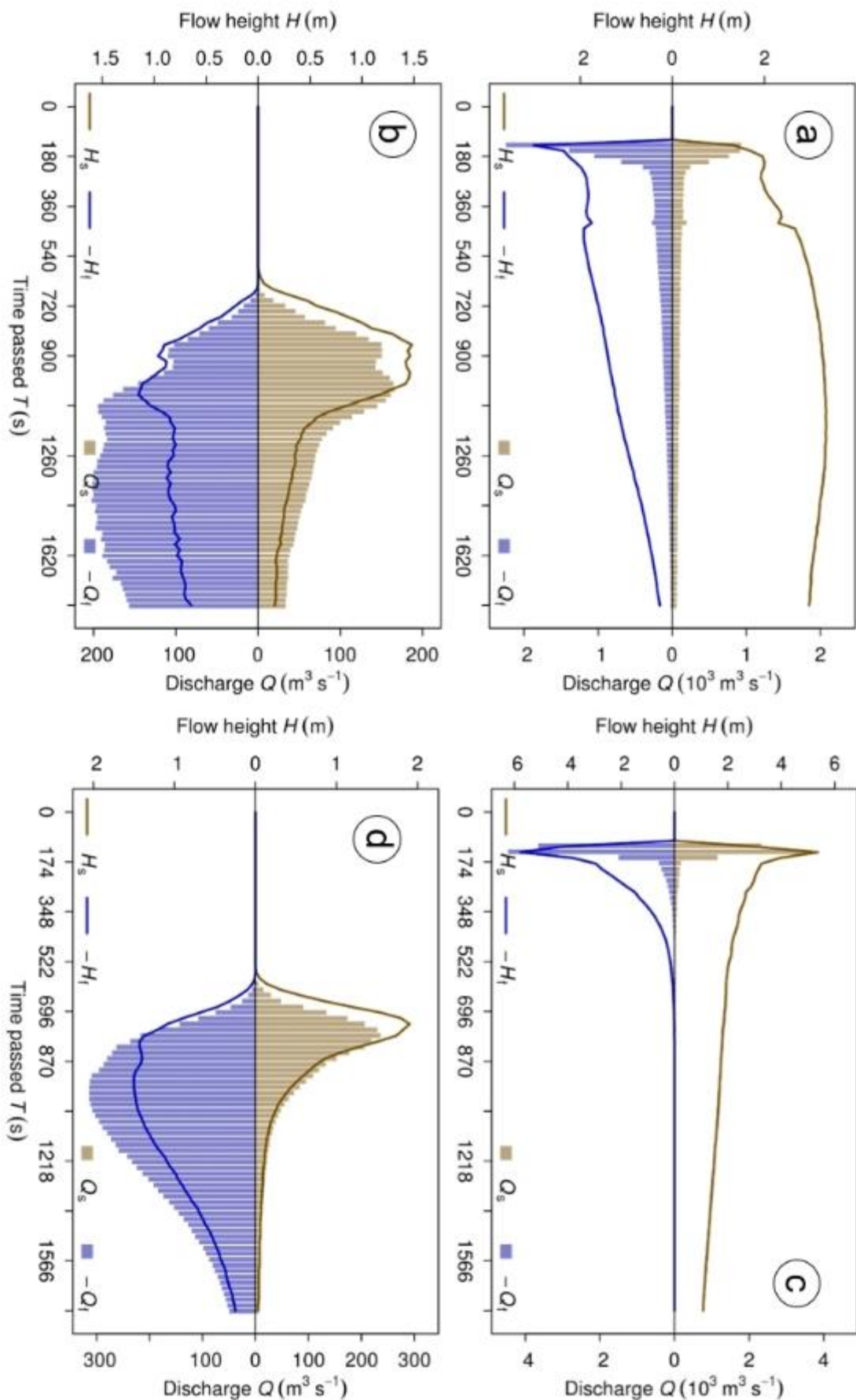
716
717 Figure 7. Overview of the heights and entrainment areas as well as the zonation performed as the basis
718 for the simulation with r.avaflow. Injection of pore water only applies to the Scenario A. The zones A–F
719 represent areas with largely homogeneous surface characteristics. The characteristics of the zones and
720 the model parameters associated to each zone are summarized in Table 1 and Fig. 4. O1–O4 represent
721 the output hydrograph profiles. The observed rock avalanche terminus was derived from WSL (2017).
722



723
724
725

Figure 8. Maximum flow height and entrainment derived for Scenario S1. RA = rock avalanche; the ob-
served RA terminus was derived from WSL (2017).

726

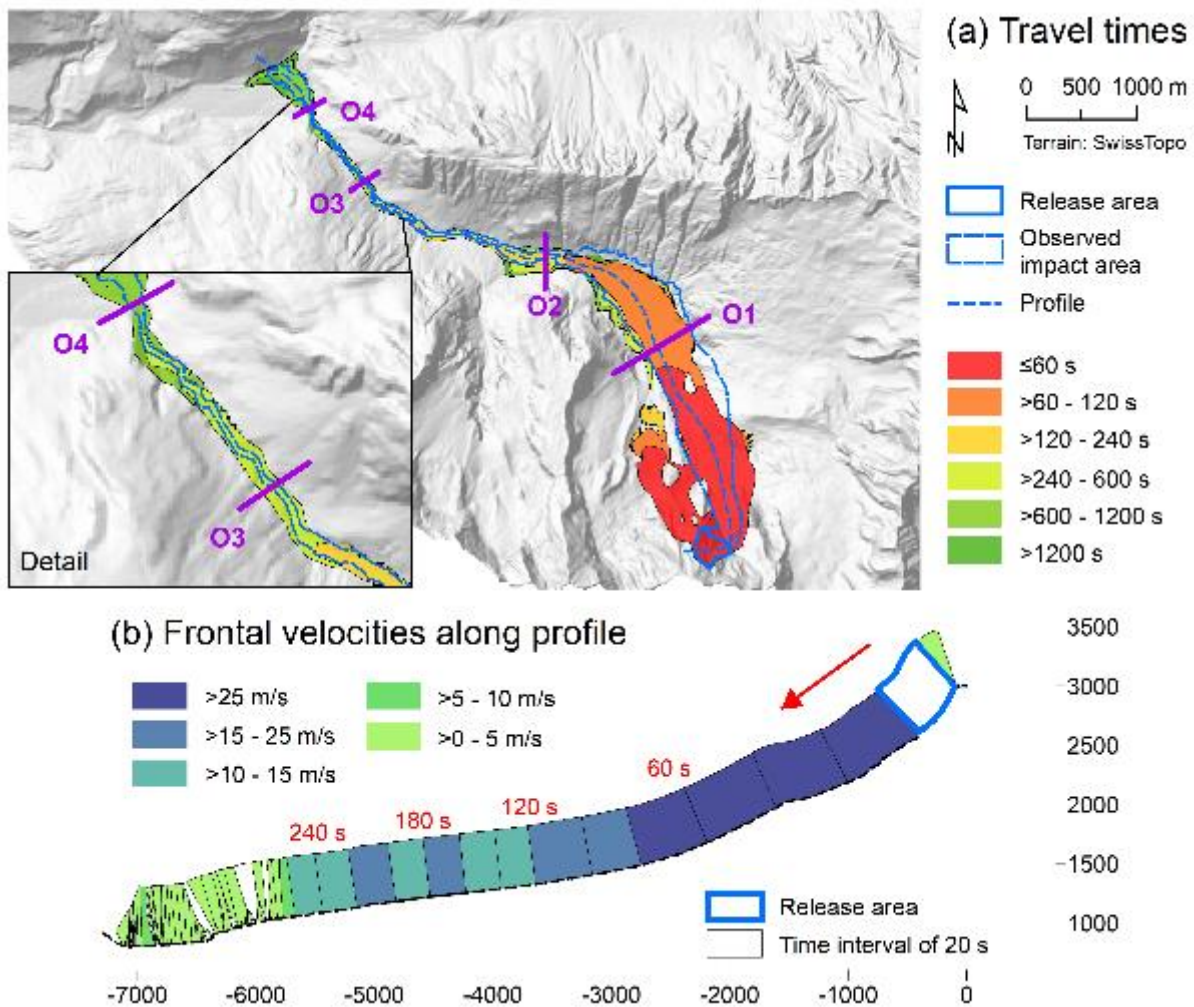


727

728 Figure 9. Output hydrographs OH2 and OH4 derived for the scenarios S1 and S2. (a) OH2 for Scenario
 729 S1. (b) OH4 for Scenario S1. (c) OH2 for Scenario S2. (d) OH4 for Scenario S2. See Fig. 7 and Fig. 8 for

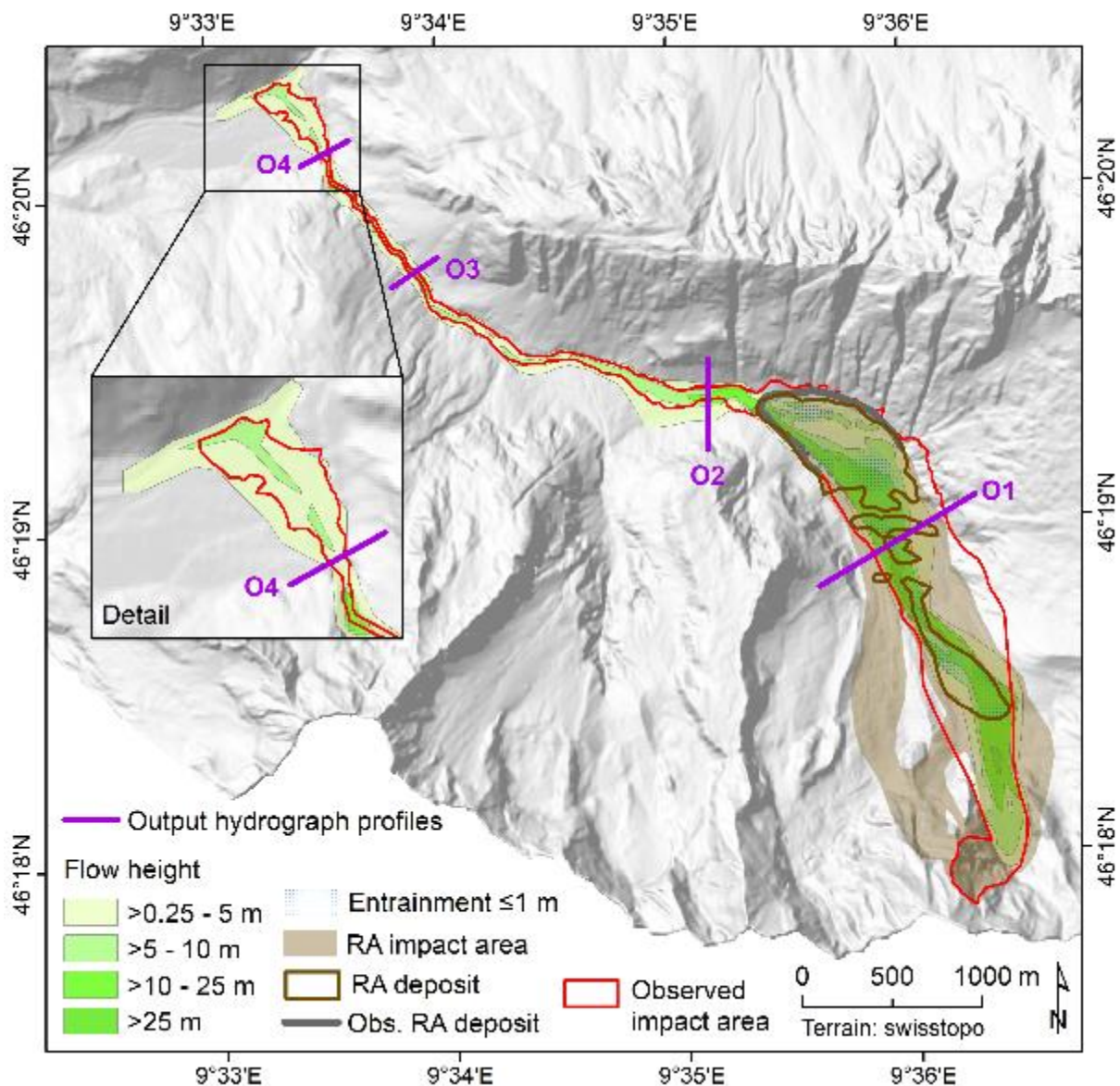
730 the locations of the hydrograph profiles O2 and O4. H_s = solid flow height; H_f = fluid flow height;
731 Q_s = solid discharge; Q_f = fluid discharge.

732



733
734 Figure 10. Spatio-temporal evolution and velocities of the event obtained for Scenario S1. (a) Travel
735 times, starting from the release of the initial rock slide-rock fall. (b) Frontal velocities along the flow
736 path, shown in steps of 20 s. Note that the height of the velocity graph does not scale with flow height.
737 White areas indicate that there is no clear flow path.

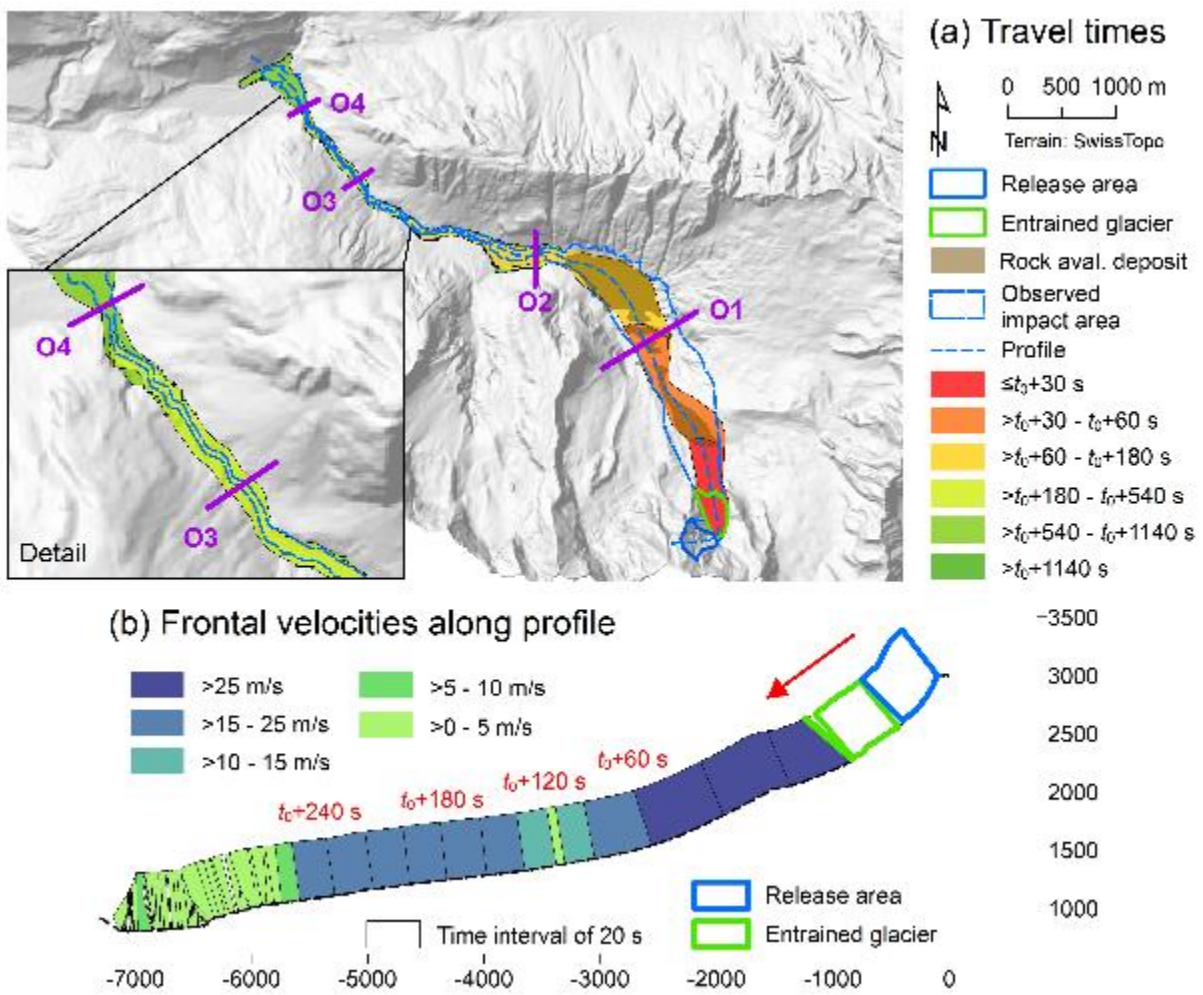
738



739
740
741

Figure 11. Maximum flow height and entrainment derived for Scenario S2. RA = rock avalanche; the observed RA terminus was derived from WSL (2017).

742



743
744 Figure 12. Spatio-temporal evolution and velocities of the event obtained for Scenario S2. (a) Travel
745 times, starting from the release of the initial rock slide-rock fall. Thereby t_0 (s) is the time between the
746 release of the rock slide-rock fall and the mobilization of the entrained glacier. (b) Frontal velocities
747 along the flow path, shown in steps of 20 s. Note that the height of the velocity graph does not scale
748 with flow height. White areas indicate that there is no clear flow path.

749